Inhibiting SOX18 with propranolol restores vascular integrity in NR2F2-driven malformations

Matthew S. Graus[1,2]*, Sawan Kumar Jha[3]*, Jieqiong Lou[4], Annegret Holm[5], Yew Yan Wong[1,2], Tara Davidson[1,2], Paul Coleman[1], Ella Sugo[6], Winnie Luu[1], Tara Karnezis[7], Jennifer Gamble[1], Geoff McCaughan[2], Scott Nightingale[6], Joyce Bischoff[5], Kazuaki Maruyama[8], Elizabeth Hinde[4], Kristy Red-Horse[3,9,10,11]†*and Mathias Francois[1,2]†*

[1] The University of Sydney, School of Medical Sciences, Sydney, New South Wales, 2006, Australia.

[2] The Centenary Institute, The Genome Imaging Centre, Royal Prince Alfred Hospital, Sydney, New South Wales, 2006, Australia.

[3] Stanford University, Department of Biology, Clark Center, 318 Campus Drive, Stanford, E350, CA 94305, USA.

[4] The University of Melbourne, School of Physics, Melbourne, Victoria, 3010, Australia.

[5] Vascular Biology Program, Department of Surgery, Boston Children's Hospital, Harvard Medical School, Boston, MA, United States

[6] Hunter New England Health, John Hunter Hospital, Lookout Road, New Lambton Heights, NSW 2305, Australia.

[7] Gertrude Biomedical Pty Ltd., Bio21, Melbourne, Victoria, Australia.

[8] Department of Pathology and Matrix Biology, Graduate School of Medicine, Mie University
2-174 Edobashi, Tsu, Mie 514-8507, Japan.

[9] Stanford Cardiovascular Institute, Stanford, CA 94305, USA.

[10] Institute for Stem Cell Biology & Regenerative Medicine, Stanford University, Stanford, CA 94305, USA.

[11] Howard Hughes Medical Institute, USA.

*Authors have contributed equally to this work

†Correspondence should be address to

Kristy Red-Horse (Tel: +81-92-642-6882)

kredhors@stanford.edu

Mathias Francois (Tel: +61 28627 9497)

mathias.francois@sydney.edu.au

One-sentence summary: Pharmacological blockade of SOX18 with Propranolol to treat a vascular anomaly caused by NR2F2 mutation.

Keywords: transcription drug, SOX18, NR2F2, transcription factor, live imaging, single molecule, stem cell, repurposing, vascular anomalies, endothelial cell

Abstract

Genomics has advanced our ability to identify disease-causing mutations, but translating this information into treatments remains challenging, particularly for rare genetic diseases. Key challenges remain, including understanding how variants of unknown significance (VUS) disrupt molecular and cellular function and how to treat perturbed physiology. Here, we identify a *de novo* heterozygous mutation in the NR2F2 gene, a regulator of venous endothelial cell identity, which causes an orphan paediatric syndrome, characterized by leaky, aberrant vascular development. Functional validation in human embryonic stem cells carrying the proband's mutation uncovers venous differentiation defects. NR2F2 is a nuclear receptor that can form dimers and recruits other transcription factors to modulate the venous gene expression program. Through *in silico* modelling and live-cell molecular imaging, we demonstrate that the NR2F2 variant protein is hypermobile, unable to form homodimers, and fails to recruit a critical partner, SOX18, thereby disrupting the venous transcriptional program. Multi-omics analysis further identifies an opposing yet coordinated regulation of common target genes by SOX18 and NR2F2 in venous endothelial cells. Here, we posit that inhibiting SOX18 activity may mitigate NR2F2 dysfunction. Remarkably, SOX18 pharmacological blockade shows a rescues NR2F2 loss-of-function in hESC-derived venous endothelial cells. Treatment with an FDA-approved drug known for its off-target SOX18 inhibition led to significant reduction in haemorrhaging resulting in a significant increase in quality of life. This proof of concept identifies a postnatal therapeutic window, coinciding with vascular plasticity during organ maturation that can be leveraged to manage vascular anomalies through successful drug repurposing.

Introduction

De novo genetic variants have been implicated in the development of vascular malformations, with a prevalence of 1.2% to 1.5% in children[1,2]. Each disease needs to be assessed individually to identify genetic vulnerability and elucidate the etiological components to determine treatment options. For this reason, developing assays to perform functional validation alongside next-generation sequencing technologies is essential to discovering biology associated with variants of unknown significance (VUS) and, therefore, potentially providing patients with personalized therapeutic options. There is a growing interest in VUS that alter the activity of genome effectors such as transcription factors (TFs), which are key molecular switches essential to proper embryonic development. Failure of these TFs to carry out their functions often leads to lethal outcomes, due to defects that impair the cardio-vascular system and endothelial cell differentiation or function[3,4]. Here, we focus on a new *de novo* mutation in a venous specific TF and the functional characterisation of this genetic insult.

The nuclear receptor subfamily 2 group F member 2 (COUPTFII/NR2F2) is a TF required for vein development in embryonic mice, zebrafish and xenopus[5–9]. Genetic disruption approaches have demonstrated that homozygous loss of NR2F2 is embryonically lethal, and heterozygous loss is attributed to vascular anomalies[10,11]. It can also block the natural vein to artery transition required for coronary artery formation[12]. Although much less known about its function in human vein development, it may be essential for life since it has a probability of being loss-of-function intolerant (pLI = 0.99, Genome Aggregation Database (gnomAD) v 4.1.0). Due to the inflexibility of NR2F2 variants, many are associated with or are genetic components of several human diseases, including congenital heart disease (CHD)[13–15] and congenital diaphragmatic hernia (CDH)[16], among other developmental defects[17].

Evidence shows that NR2F2 supports venous endothelial cell (EC) differentiation though two potential mechanisms: 1. Regulating cell identity genes—promoting venous and inhibiting arterial genes [5,18,19] and 2. enhancing cell cycle genes[12,18,19]. Deletion of one copy in coronary ECs during embryonic development drastically decreases EC numbers and proliferative capabilities[12]. Part of NR2F2 activity is modulated by interactions with protein partners such as GATA2 or NK2-3 [20,21]. In addition, NR2F2 cooperates with the SOX18[22,23] TF in venous progenitor cells, to initiate the early steps of lymphatic EC specification[24].

SOX18 is a member of the SOX (SRY-related HMG-box) family of TFs that is essential for different aspects of EC differentiation. Its been shown to regulate control of vessel calibre via genetic cross talk with VEGF-D[25] and influences regulation of EC contact[26,27]. During embryogenesis, SOX18 expression is essential to induce the early steps lymphatic specification[28] but is downregulated once the blood and lymphatic vascular network are established. However, under pathological conditions in adults, SOX18 is reactivated and plays a role in modulating endothelial progenitor cell differentiation during solid

tumour growth[29–31]. Consequently, mutations in SOX18 have been identified for their involvement in rare human vascular disorders, including hypotrichosis-lymphedema-telangiectasia-renal syndrome (HLTRS)[32,33] and cancer metastasis[34]. Beyond these conditions, SOX18 also has been shown to play a role in the formation of aberrant vasculature as seen in infantile hemangioma (IH), a vascular neoplasm characterized by rapidly growing, aberrant vessels. Notably, SOX18 has been shown as a key regulator of hemangioma stem cell to hemangioma endothelial cell differentiation[35,36]. This is further supported by the development of a small molecule inhibitor, SM4[22,37] and that two FDA-approved therapies (propranolol and atenolol) are currently used to treat IH[35,36,38], providing compelling evidence of SOX18's involvement with pathological ECs differentiation and highlighting its potential as a therapeutic target.

In this study, we use next-generation sequencing and *in silico* modelling combined with a suite of live-cell, quantitative molecular imaging techniques, and human embryonic stem cell (hESC) to human vascular endothelial cell (hVEC) differentiation assays to characterize a *de novo* heterozygous NR2F2 mutation identified in a proband. Our approach rapidly determines that the VUS drives a loss-of-NR2F2 function, causing venous differentiation defects through atypical molecular behaviour and disruption to protein-protein interactions with SOX18. Identification of a SOX18-NR2F2 antagonistic regulatory layer of the arterio-venous program prompted us to use a pharmacological rescue of NR2F2 loss-of-function via SOX18 blockade in a model of hESC to hVEC differentiation. This finding elucidates a SOX18-dependent molecular mechanism underlying Propranolol's interference with NR2F2 dysfunction in a clinical setting, as it has been successfully used to pharmacologically manage the proband's condition.

Results

A *de novo* NR2F2 variant is identified in a novel vascular anomaly

In this study, a five-year-old proband was diagnosed with multiple vascular lesions that radically impacted development and quality of life. Early indications of the disease manifested as recurrent gastrointestinal haemorrhages, commencing when the patient was a newborn. Other clinical features of the disease became apparent as the proband developed. These include multiple gastric and small bowel mucosal vascular lesions characterized by increased number of ectopic vessels and dilated capillaries, non-cirrhotic portal hypertension associated with hepatofugal flow, and diffuse hepatic arterioportal blood shunting that did not respond to surgical shunt treatments (Fig 1 A-C). Due to the gastrointestinal haemorrhages, a porta-cath was necessary for regular blood and iron transfusions, and plans were underway to list for a liver transplantation by pre-school age.

Owing to the rarity and severity of the disease and its resistance to treatment, whole exome sequencing was performed and found a heterozygous VUS in exon 3/3 of the NR2F2 gene (c.994del (G), p.Ala332Pro). Review of the online mendelian inheritance in man (OMIM) entry for NR2F2 identified that one of the clinical features of the NR2F2 phenotypes is epicanthus inversus (eye lid fold defects) which is a relatively uncommon clinical feature and was also observed in this proband. This prompted us to focus our analysis further on this NR2F2 variant. The variant (NM_021005.4), Chr15 (GRCh38): g.96337371del, causes a frame-shift and amino acid change from an Ala to Pro at position 332 (Supp Fig 1A), resulting in a scramble and truncation of the ligand binding domain (LBD) (Fig 1D). This c994del variant has not been reported previously, making it clinically novel. Previous NR2F2 deleterious variants have been identified and shown to cause a wide range of symptoms ranging from cardiac to sex determination defects[13–15,17] unlike this VUS which seems specifically involved with severe vascular defects.

To investigate the molecular mechanisms driving the phenotypic changes observed in the proband, we used AlphaFold 3 [39,40] to perform *in silico* modelling to examine how the frameshift mutation affects the LBD conformation. Structural analysis of the $NR2F2^{WT}$ LBD determined that this region is critical for its homo-dimerization[41]. The modelling revealed the $NR2F2^{c994del}$ variant exhibits an abnormal folding confirmation compared to the $NR2F2^{WT}$, starting after amino acid 332, leading to a loss of residues in the form of α-helices that are involved in dimerization (Fig 1E, Supp Fig 1B).

Whole exome sequencing also detected a hemizygous variant in MAP7D3 (c.1783dupA, p.Met580Asnfs*4). The variant is found in exon 10/19 of MAP7D3 gene (NM_024597.4), ChrX (GRCh38): g.136230397dup, which causes a frameshift and is expected to result in a nonsense mediated mRNA decay. This variant has been found in other individuals and is not considered a ClinVar variant on gnomAD (Genome Aggregation Database (gnomAD) v 4.1.0). The MAP7D3 gene has not been reported as key regulator of vascular development and there is no literature on the role of this factor in the endothelium. Therefore, we opted for an investigation that centers on a cell autonomous role of NR2F2 (COUPTFII) dysfunction, which is a well-known regulator of venous EC identity during embryogenesis.

Mutations in key developmental TFs specific to EC development have been reported to cause rare vascular diseases[44,45]. Mutations in the transactivation domain of SOX18 TF are known causes of HLTRS, which has a dominant-negative effect and suppresses the endogenous function of the wild type protein[23,46,47]. Remarkably, the FDA-approved drug propranolol has shown considerable efficacy in enhancing the clinical management of the HLTRS syndrome[36]. Since the early 2010s, this drug has been primarily used as the first-line treatment for IH, the most common vascular tumor, whose mechanism of action also relies on SOX18 inhibitory activity[35,36,38]. Given propranolol's established safety for use

in paediatric vascular disorders, the identification of its recent mode of action via SOX18 blockade, and the worsening condition of the proband with limited therapeutic options, a decision was made to use propranolol to manage the proband's condition.

Treatment and recovery

Propranolol treatment started at a dose of 1.5mg/ml/kg in August 2021. By December 2021 haemorrhaging had resolved, and haemoglobin levels stabilized, resulting in the patient no longer requiring transfusions (Fig 1F). In early 2023, a Doppler ultra-sound was performed and it determined that hepatopetal flow had been restored (Fig 1G). Due to the proband no longer requiring transfusions the porta-cath was removed, and the liver transplant was cancelled. At the time of writing this study the treatment has been a success, with the probands' quality of life drastically improving, allowing for a return to a more normal and fulfilling life over the past 4 years. Following the successful treatment outcome, we aimed to unravel the underlying cellular and molecular mechanism of the propranolol's therapeutic effect.

NR2F2^{c994del} impairs venous but not arterial differentiation

The proband's successful treatment exemplifies the application of diagnostic reasoning, encompassing the identification of multiple symptoms, integration of clinical genomics, and implementation of propranolol therapy (Fig 1H). We started by investigating the pathogenicity of the NR2F2 variant. Given its importance for vein identity in model organisms, we tested the impact of the variant on vein EC differentiation in a highly efficient human stem cell differentiation model of venous and arterial EC generation[48] (Fig 2A). We generated H1-hESC lines containing the proband-specific variant in a homozygous fashion (Fig 2A, Supp Fig 1A,C). Western blotting confirmed that the NR2F2^{c994del} lines had NR2F2 proteins at comparable expression to wild type but, as expected at a lower molecular weight (predicated NR2F2^{WT} = 45.5kDA (414AA) and NR2F2^{c994del} = 41.03kDA (377 AA), consistent with a premature stop codon. (Supp Fig 1D).

To assess the phenotypic impact of the NR2F2 variant and its cell autonomous role, we differentiated wild type control and NR2F2^{c994del} lines into vein and artery ECs. The differentiation assay used FACS and qPCR readouts to assess cellular and molecular levels of arterial and venous differentiation markers (vein=CD73, *APLNR*, *NRP2*, and SOXFs). In line with its known role as a hallmark of venous identity, NR2F2^{c994del} caused an increase in the overall number of immature ECs (Fig 2B), and resulted in a significant decrease in terminal venous differentiation (Fig 2C, CD73+ ECs, Supp Fig 2E-F). QPCR analysis of venous markers, *APLNR*, *EPHB4*, and *NRP2* further validated FACS observations with significantly decreased venous marker expression (Fig 2D). This loss of venous identity was not paralleled by a concomitant increase in markers of the mature arterial endothelium such as Sox17 (Fig 2E). The lack of change in the Sox7 and Sox18 expression in the NR2F2 variant clones suggested that

this TF is not directly upstream of SOXF members in the model of venous differentiation (Fig 2E). In contrast to its effect on veins, NR2F2^{C994del} did not influence the arterial differentiation process (Fig 2F). Of interest is the finding of a larger proportion of ECs lacking artery or vein identity trends with the patient duodenum tissue sample showing an increased number of ectopic, thin-walled vessels (Fig 1B). These findings show that the NR2F2^{c994del} variant can autonomously interfere with EC subtype differentiation, specifically within the venous compartment.

Molecular mechanism of NR2F2^{c994del} impaired function

Because the proband is heterozygous and has both wild type and variant alleles expressed, we modelled the effect of this abnormal configuration on homodimer formation. Crystal structure studies of the LBD of NR2F2^{WT} further confirmed the dimerization residues involve several α-helices, including 7 (amino acids 297-301), 8 (amino acid 378), 9 (amino acids 335 and 339), and 10 (amino acids 358-372), along with the loop between α-helices 8 and 9 (amino acids 323 and 324)[41]. Because the location of the frame-shift in the c994del variant occurs at amino acid 332, the dimer residues are lost, resulting in an abnormal folding conformation of the C-terminus. As expected, the *in silico* modelling indicates the loss of the dimer residues results in the inability of the variant and WT to form a dimer. The VUS in a disordered conformation likely creates an unstable interface compared to NR2F2^{WT} (Fig 3A, Supp Fig 2A-C), which could result in a global destabilization of the NR2F2 protein pool.

To functionally validate these modelled predictions, we used a combination of quantitative molecular imaging approaches to assess protein-protein interactions and protein mobility in living cells at single-molecule resolution[23]. Cross raster image correlation spectroscopy (cRICS) measures the co-diffusion of two proteins and number and brightness (N&B) measures the oligomeric state of the proteins, enabling the measurement of protein-protein interactions in real-time. By contrast, single molecule tracking (SMT) measures the mobility and proportion of diffusing proteins, as well as their temporal occupancy[49–52]. To compare biophysical behaviour between the WT and c994del variant, we imaged an over-expressed, Halo-tagged version of either NR2F2^{WT} or NR2F2^{c994del} in live ECs (description of imaging methods in [23], Supp Fig 1).

Consistent with the observed model, cRICS and N&B imaging showed the NR2F2^{c994del} variant lost its ability to co-diffuse and form homo-dimers (Fig 3B-C). Following on, we next investigated how the loss of homo-dimerization affects the variants ability to navigate and interact within the nuclear environment. SMT imaging determined that most of the variant population has an increased diffusion profile compared to its WT counterpart (Fig 3D-E (HeLa), Supp Fig 2D-H (HUVEC)). Taken together, the data indicates that the variant is unable to homo-dimerize, allowing the vast majority of NR2F2^{c994del} molecules to diffuse as monomers, hence dramatically impacting the total pool of NR2F2 available to perform its function. We next assessed whether homo-dimerization is necessary for NR2F2 to bind and

interact with its environment. Temporal occupancy SMT established that the variant spends less time searching for binding sites (Supp Fig 2F), but a similar amount of time interacting when an interaction occurs (Supp Fig 2G). Additionally, the variant has a much smaller proportion of the population bound at any time (Supp Fig 2H). These results demonstrate that the variant causes interactions to be less stable through the loss of target gene search pattern and less of the population undergoing longer specific interactions with the chromatin (summary of the variant biophysical features in Table 1).

The biophysical characterization of the defects establishes that the c994del variant severely disables NR2F2 activity and interferes with its physiological and molecular function, leading us to define the variant as a loss-of-function variant. These findings prompted us to explore whether NR2F2 defects might interfere with other key regulators of venous identity, akin to the mechanism reported for the SOX18 dominant-negative mutation[23].

A discrete pool of venous endothelial cells co-express NR2F2 and SOX18 *in vivo* during embryogenesis and endothelial dysfunction.

We next questioned whether the variant also impacts NR2F2's capacity to hetero-dimerize with a known protein partner. Previous studies have shown direct interaction of NR2F2 and SOX18 in cell based assays[22,23], and it is known that these two TFs together induce PROX1 expression in the venous endothelium to specify lymphatic endothelial cells[24]. Further, analysis of a scRNA-seq dataset of hESCs[48] that are differentiated into either arterial or venous ECs, as well as a scRNA-seq atlas of mouse embryos at E8.5,[53] identifies a subset of the venous population that co-express NR2F2 and SOX18 (Supp Fig 3A, B).

Since NR2F2 and SOX18 are co-expressed in a subset of hESC-derived venous ECs, we next sought to determine whether these two TFs are co-expressed *in vivo* in humans. We started by investigating the expression profile of NR2F2 and SOX18 in a human embryo at CS17 (gestational age: 42-44 days) and in the pathological endothelium of IH, venous malformations (VM), and arteriovenous malformations (AVM). During physiological vascular development, immuno-fluorescence staining revealed that ECs co-expressing both TFs can be found in the liver, gut, aorta, and cardinal vein junction (Fig 4A, Supp Fig 3C(A-D")). Further assessment of NR2F2 and SOX18 co-expression in endothelial nuclei is a constant feature among the vascular anomaly entities IH, VM, and AVMs (Supp Fig 3D-F). This finding led us to examine whether the proband exhibits a similar co-expression profile of these two TFs.

Examination of the proband's liver and duodenum (polyp) tissue samples revealed co-expression of NR2F2 and SOX18 in CD31-positive vessels (Fig 4C-D). Two subsets of vessels were observed; one that only express SOX18 (most likely arteries based on their morphological features) and the other co-

express both NR2F2 and SOX18 (most likely veins based on the expression of NR2F2 and morphological features) (Fig 4C-D", Supp Fig 4A-B). The co-expression of these two regulatory factors specific to the endothelium raises the question whether a direct interplay or protein crosstalk would affect their activity.

Defective NR2F2 disables NR2F2-SOX18 interplay.

To explore the interaction between NR2F2 and SOX18 directly we modelled the hetero-dimerization using Alphafold 3 (Supp Fig 4A-B)[39,40]. Modelling the dimerization of NR2F2^{WT} and SOX18 predicted the binding interface between the two TFs, albeit with very low confidence scores. The modelling predicts that the binding interface to be in the DNA binding domain (DBD) of NR2F2 (~ amino acid 95-97) and in the central transactivation domain (TAD) of SOX18 (~ amino acid 226-235) (Supp Fig 4A, left). Modelling of NR2F2^{c994del} and SOX18 found the DBD on NR2F2 and the TAD on SOX18 to be farther apart/not interacting (Supp Fig 4A, right).

To validate the *in silico* prediction of this hetero-dimer, we performed cRICS, N&B, and SMT on either NR2F2^{WT} or NR2F2^{c994del} halotag in the presence of SOX18-dendra or the reciprocal condition, SOX18-dendra in the presence of either NR2F2^{WT} – halotag or NR2F2^{c994del} – halotag. Co-diffusion analysis of NR2F2 using cRICS imaging identified a loss of homo-dimer formation for NR2F2^{WT} when in presence of SOX18. This demonstrates a direct interaction between the two TFs and a competitive mechanism at play; however, there was no change in homo-dimer co-diffusion for NR2F2^{c994del} in the presence of SOX18 (Fig 5A). Hetero-dimer formation measured by N&B indicated a significant loss of dimer formation for the NR2F2 variant compared to WT (Fig 5B). To understand how hetero-dimerization affects the diffusion profile of both TFs, we turned to SMT. This approach revealed when SOX18 is present NR2F2^{WT} becomes more diffusive (Fig 5C-D). By contrast, SOX18 mobility profile is more confined in the presence NR2F2 wild type (Fig 5E-F). Both observations argue in favour of a competitive binding behaviour between these two TFs. In addition, the presence of SOX18 does not influence the mobility of NR2F2^{c994del} (Supp Fig 4B-C). We find that NR2F2^{c994del} does not meaningfully change SOX18 mobility profile (Fig 5E-F). Taken together, the imaging suggests that NR2F2^{WT} and SOX18 directly interact, whereas, the NR2F2^{c994del} variant most likely influence SOX18 mobility indirectly through the interference with its wild type counterpart (summary of NR2F2/SOX18 interplay in Table 2). Characterising this interplay between SOX18 and NR2F2 prompted us to posit whether a co-modulated gene regulatory network can be defined in the venous vasculature.

NR2F2 and SOX18 antagonistically regulate a subset of genes to govern arteriovenous identity

To explore a potential coordinated regulation between NR2F2 and SOX18, we integrated two previously published RNA-seq datasets, comparing known EC identity genes. The first column examines HUVECs that have had NR2F2 knocked out (KO) and the second dataset examines HUVECs

that were treated with a SOX18 small molecule inhibitor, Sm4[19,23] (Supp Fig 4D). Surprisingly, we observed that the gene response to the perturbed activity of one TF consistently leads to an opposite response when the other transcription factor loses its function. This antagonistic response for a subset of specific arteriovenous markers prompted us to expand our analysis to a larger gene set. To determine common target genes for these two TFs on a genome wide scale, we combined four publicly available NR2F2 and SOX18 ChIP-seq data sets[19,23] with ChiP-seq datasets for marks of active gene expression (e.g. H3K27ac and H3Ke4me3 ENCODE consortium[54]) and intersected these peaks with ATAC-seq results from HUVECs that were either untreated or treated with Sm4[22,37] (Fig 5G). This approach enabled us to identify regulatory regions that are SOX18/NR2F2 co-bound and that change their accessibility upon SOX18 inhibition. We identified 139 regions with enhancer like signature (ENCODE cCRE[54] and H3K27ac, Supp Fig 4E, yellow bar and light blue track) that are recruited by SOX18 and NR2F2 and less accessible upon SM4 treatment (Supp Fig 4E, green bar). Peak to gene analysis[55,56], assigned these enhancers to probable transcription start sites (TSS) and revealed 245 target genes (Supp Table 1). Cross checking known markers from that reference gene list, with a publicly available scRNA-seq dataset of hESC to endothelial differentiation[48] reveals that both SOX18 and NR2F2 potentially co-regulate the arterio-venous program (Supp Fig 4E) and narrowed down the list of candidate genes to 70 genes with an arterial or venous specific expression profile (Supp table 2).

To further validate SOX18-dependency of these 70 target genes, we performed qPCR analysis on HUVECs treated with Sm4. This approach determined that these genes are either trans-activated or repressed by SOX18 (Supp Table 3). Next, we set out to validate NR2F2/SOX18 co-regulation for a random subset (Fig 5H, yellow box) of these 70 genes using qPCR analysis after the pharmacological inhibition of either NR2F2 alone with CIA1[57] or SOX18 alone with Sm4 or using a combination of both small compounds (e.g Sm4 + CIA1) (Fig 5I, Supp Fig 4F). A striking feature of the gene expression profiles under different treatments was a clear opposite response to either the NR2F2 inhibition or the SOX18 blockade. When cells were treated in presence of both inhibitors there was a consistent pharmacological rescue by SOX18 inhibitors on NR2F2 dysregulated targets. These observations strongly suggests that NR2F2 and SOX18 jointly regulate a subset of shared target genes in an antagonistic manner.

Taken together, the antagonistic regulation between NR2F2 and SOX18 on a subset of arterial promoting genes, along with their direct molecular interactions, led us to hypothesize that the loss of NR2F2 function caused by the proband's variant could potentially be reversed by inhibiting SOX18 activity, thereby restoring the balance in the transcriptional output of these two factors with opposing roles.

Drug repurposing and molecular mechanism of treatment

Recent findings have demonstrated that both propranolol and SOX18 small molecule inhibitor SM4 inhibit the differentiation of hemangioma stem cells into hemangioma endothelial cells in a SOX18-dependent manner[35,36,38,58]. In particular, propranolol is composed of a R(+) and S(-) enantiomer mixture at a (1:1) equimolar ratio with the R(+) enantiomer (R(+)propranolol) devoid of beta-adrenergic effects. Previous research has demonstrated the R(+) enantiomer is capable of disrupting SOX18 activity [35,36,59,60]. Given that NR2F2 and SOX18 are co-expressed in the same vascular beds and antagonistically co-regulate a common subset of arterial related genes, we sought to determine whether R(+)propranolol-induced SOX18 inhibition has the potential to rescue NR2F2 loss-of-function caused by the variant $NR2F2^{c994del}$.

Taking advantage of molecular imaging, we first evaluated if R(+)propranolol directly engages with NR2F2 by measuring its molecular mobility and temporal interaction times using SMT and N&B quantitation. This approach firmly established that R(+)propranolol (Rprop) does not directly interfere with NR2F2 (Supp Fig 5A-F) since it does not disrupt a broad range of key biophysical features. Because R(+)propranolol does not disrupt NR2F2 mobility or dwell time profiles, we next examined the effects of this compound on NR2F2-SOX18 interactions. Using a co-expression experimental setup of these two TFs, we introduced R(+)propranolol treatment. In absence of the drug, SMT imaging revealed the presence of SOX18 increases the proportion of diffusing $NR2F2^{WT}$ molecules compared to $NR2F2^{WT}$ alone, suggesting that SOX18 is sequestrating NR2F2 away from its chromatin-bound pool. Additionally, when SOX18 activity is disrupted by R(+)propranolol, we observed a decrease in the proportion of diffusing $NR2F2^{WT}$ molecules indicating that R(+)propranolol interference with SOX18 restores the chromatin-bound fraction of $NR2F2^{WT}$ to its baseline state (Fig 6A-B). Conversely, there is little change in $NR2F2^{c994del}$ diffusion profile in presence of SOX18 with or without R(+)propranolol (Supp Fig 5G-I). This indicates that the protective effect of R(+)propranolol is meditated at a molecular level specifically by modulating indirectly the availability of the $NR2F2^{WT}$ pool through an interference via SOX18 activity. In other words, this work builds on previous findings that inhibition of SOX18 by pharmacological blockade reduces NR2F2 and SOX18 interaction[37] and establishes that SOX18 inhibition favours an increase of $NR2F2^{WT}$ activity on the chromatin (summary of drug mode of action, Table 3). Having elucidated that R(+)propranolol-induced SOX18 inhibition restores a vast proportion of the $NR2F2^{WT}$ behaviour, we next investigated whether R(+)propranolol is able to rescue the venous phenotype caused by the NR2F2 variant in a human pre-clinical model of stem cell to endothelial cell differentiation.

R(+)propranolol effects are endothelial cell autonomous and rescues venous defects caused by $NR2F2^{c994del}$

To perform an orthogonal validation of data obtained from the single molecule imaging, we next took advantage of the hESC to venous EC differentiation assay. The experimental design relies on a

differentiation protocol in the presence or absence of SOX18 blockers (either Sm4 or R(+)propranolol) when cells are transitioning from vein intermediates (D3) to vein (D4). (Fig 6C). SM4 and R(+)propranolol treatment rescued the terminal differentiation defects of the venous population caused by the NR2F2 variant (Fig 6D, Supp Fig 6A). Further validation of this rescue was shown at a molecular level by analysing vein specific markers (Fig 6E). Based on the hESC to EC validation, we determine that the R(+)propranolol molecular mechanism specifically acts on the venous endothelium and suggests that SOX18 inhibition in the proband has led to a restored physiological function of the venous vasculature.

Discussion

The challenge of managing VUS in rare diseases

The uniqueness of this case resides in the fact that only the vasculature seems severely affected. In contrast, no other physiological defects were detected in the developing heart, lungs, brain, or gonads, as is often the case with NR2F2 VUS. The exemplar illustrates the challenge of dealing with pathophysiological mechanisms that underpin a rare disease. There are loss-of-function mutations in a wide range of genes that can result in variable phenotypes, and learning why they do so remains one of the major roadblocks to improve clinical management of these conditions. This emphasizes the importance of understanding molecular mode of action in a cell-type specific context to unlock viable therapeutic options.

Leveraging quantitative molecular imaging to improve functional validation

This study builds upon the current model of personalized medicine by incorporating clinical diagnostics, genetic profiling, *in vitro* genetic studies, and precision drug therapy for the benefit of the patient. For the first time, we propose to extend this beyond the current approach by incorporating quantitative molecular imaging. This allows us to assess the molecular mode of action of protein mutations, on-target engagement of a protein partner, and known inhibitor. This integration enabled the ability to rapidly establish therapeutic proof of utility and drug repurposing potential in a rare vascular disease. Here, we propose that, in addition to the utility of genomic technologies for diagnostics, a complementary approach focused on functional validation with quantitative molecular imaging is essential and should be considered as a tool to uncover molecular mechanisms and reveal new treatment options to improve clinical outcomes.

Using molecular imaging to investigate pharmacological on-target engagement

Targeting TFs to modulate gene expression has been studied for decades. Historically, TFs have been considered “undruggable” due to their intrinsic disordered domains, lack of traditional drug binding pocket, and dynamic nature[61]. This study highlights the potential of using quantitative molecular imaging as a strategy to perform on-target engagement. Using SMT has unlocked the ability to assess a molecular target in the presence of its inhibitor[62,63]. Here, we firmly establish that R(+)propranolol mode of interference is mediated via SOX18 disruption whereas NR2F2 behavior remains unaffected by this drug. Molecular imaging thus provides a powerful tool to evaluate the interaction between drugs and molecular target, offering a direct method to validate therapies aimed at specific pathways.

An updated molecular mechanism for investigating TFs

We propose a molecular model explaining how R(+)propranolol treatment benefited the proband. Under normal circumstances, a physiological balance between NR2F2 and SOX18 ensures the coordinated transcriptional regulation of common target genes central to arteriovenous identity. However, in the

proband's case, a heterozygous variant in NR2F2 causes only half of the pool of NR2F2 molecules to function properly, leading to a shift in balance in favour of SOX18 activity. This results in transcriptional dysregulation being over-dominated by SOX18. To correct this imbalance, a molecular strategy based on SOX18 inhibition is used to compensate for the over-active pool of SOX18 and to restore a relative equilibrium between the remaining functional NR2F2 and less active SOX18 molecules (Fig 6F). Our findings introduce a novel approach to correct loss-of-function mutations by targeting TFs protein-partners, ultimately altering gene regulation. In the case of HLTRS, directly targeting SOX18 proved to have a beneficial therapeutic effect[23].

An illustration of phenotypes arising from the antagonistic relationship between SOX18 and NR2F2 is the proband's ectopic thin-walled vessels (Fig 1B). VEGF signaling is well-established as a critical pathway for angiogenesis and blood vessel maintenance[64], with DCBLD2 playing a role in VEGF signaling through its interaction with VEGFR2 [65]. Our study reveals that NR2F2 acts as a repressor for DCBLD2 while SOX18 acts as an activator (Fig. 5I). A possible explanation is that ectopic vessel formation might have arisen from the disruption in the co-regulation of DCBLD2, which in turn has dysregulated VEGF signaling. Supporting this motion, a patient with a novel homozygous nonsense mutation in DCBLD2 was found to have developed multiple cerebral AVMs[66].

More broadly, vascular anomalies have been linked to alteration in signaling pathways associated with developing arteriovenous malformations (AVM), cutaneous-mucosal venous malformations, and capillary malformation with AVMs[67]. Specific signaling components are critical for EC identity, such as NOTCH, a key marker for arterial differentiation. Notably, the loss of signaling from either NOTCH or platelet-derived growth factor subunit B (PDGFB), has been associated with the formation of AVMs[68,69]. Additionally, SOX18 has been shown to regulate NOTCH1[70,71], while KO of NR2F2 in HUVECS has been found to change expression of NOTCH2-4 and decreases PDGFB expression[19,69]. Collectively, these findings suggest that the NR2F2 and SOX18 signaling axis might be essential for regulating pathways implicated in vascular malformations. This study introduces the potential for exploiting the NR2F2-SOX18 antagonistic relationship as a novel therapeutic target for treatment of vascular malformations.

A new therapeutic pathway for congenital malformations

The findings from this work establish a clear window of opportunity for therapeutic intervention in the context of congenital malformations acquired during fetal development. Vascular malformations present a unique challenge due to their complexity and location in the body, often rendering surgical intervention impractical[72]. In such cases, pharmacological therapies are the preferred option. An example is sirolimus (rapamycin), an mTOR inhibitor, which has shown positive results in some patients[73,74]. However, because of the heterogeneity of the disease, not all individuals respond to this

therapy, highlighting the need for other pharmacological options[75]. This study suggests that blood vasculature plasticity during post-natal organogenesis, which relies on developmental pathways, can be taken advantage of to treat VUS. Here, we uncover that the balanced activity of SOX18 and NR2F2 is essential for properly developing arteriovenous identity, offering new insights into the molecular mechanisms underlying vascular malformations and new pathways that may be exploited for future therapies.

In conclusion, by taking a personalized medicine approach to study the proband's VUS, we were able to provide an informed diagnostic at molecular resolution and develop a rationale for the repurposing of one of the most widely used beta blockers. Looking forward, this path can be used as a personalized medicine approach for assessing the causes and treatments of other rare diseases.

Methods and Materials

Cell culture

Hela cells were cultured in supplemented DMEM (Gibco) with 10% FBS, 1% GlutaMAX (Gibco), 1% MEM Non-essential amino acids (MEM NEAA, Gibco). Cells were cultured at 37ºC with 5% CO_2. HUVEC cells were cultured in EBM-2 media (Lonzo) supplemented with EGM-2 bullet kit (Lonzo). Cell were cultured 37ºC with 5% CO_2.

hESC

Undifferentiated H1-hESC (Wicell, WA01) were maintained in mTeSR1 plus medium (StemCell Technologies) in monolayer culture on Geltrex (ThermoFischer Scientific, # A1413302). The medium was changed on alternate days per manufacturer guidelines. The cells were split and maintained based on previously published protocol[76].

Generation of H1-hESC with NR2F2^{c994del} mutation

H1-hESC containing NR2F2^{c994del} mutations were generated using CRISPR-Cas9 cells with synthetic gRNA (Synthego), Cas9 (Alt-R™ S.p. HiFi Cas9 Nuclease V3, IDT, #1081060) and HDR donor template (IDT). The knockin strategy and gRNA sequence, and HDR oligos sequence are shown in Supplementary Figure 1C.

H1-hESCs at 40-50% were treated with 10 μM ROCK inhibitor (Thiazovivin) 24h before the electroporation. Cells were then dissociated using Accutase, followed by dilution in DMEM/F12 (1:5) and centrifugation at 300g for 5 mins. Subsequently, cell pellets were resuspended in PBS and centrifuged at 300g for 5 mins. 200,000 cell pellets were then resuspended in 10 μl Buffer R (for each well in 24 wells plate). Cas9-gRNA complex was prepared by mixing 36μM Cas9 (final concentration) and 0.5 μl gRNA and incubated for 20 mins at RT. HDR donor oligo was added to the mix followed by H1-hESC. Cells were electroporated using the NeonTransfection system (Fischer Scientific, Invitrogen™ #MPK5000) according to manufacturer guidelines (electroporation condition: 1400V, 20ms pulse width, 1 pulse). Following electroporation, cells were transferred to the Geltrex-coated 24-well plate containing 500 μl mTeSR plus + 10 μM Thiazovivin. The medium was changed 24 hours post-transfection, followed by DMEM/F12 wash, and switched to mTeSR plus medium. Single cells were then FACS sorted (MA900), expanded, and Sanger sequenced to identify clones containing NR2F2^{c994del}.

Differentiation of H1-hESC to Artery and vein Endothelial cells

The protocol to differentiate artery and vein endothelial cells from H1-hESC has been published previously[48,76]. In short, at day 0, H1-hESCs were dissociated into single cells with Accutase (Sigma, A6964), and 175,000 cells were plated in each well of 12 wells of cell culture plates pre-treated with geltrex for 1h at 37ºC. Cells were seeded in mTeSR plus + 1μM Thiazovivin (Tocris, #3845). On day 1, cells were washed briefly with DMEM/F12 (Thermo Fischer Scientific, #11320082) and differentiated in a primitive streak induction medium. On Day 2, cells were washed briefly and differentiated in a lateral mesoderm induction medium (Day2, lateral mesoderm). For Artery differentiation, cells were briefly washed and differentiated in an Artery induction medium for 24 h. For Veins, the Day 2 lateral mesoderm induction medium was incubated in day 3 vein intermediate medium, followed by the day 4 vein medium.

Day 1: Mid primitive streak induction	Final	Stock
Activin A	30 ng/mL	50ug/ml
BMP4	40 ng/mL	100ug/ml
CHIR99021	6 µM	10mM (10mg/2.15ml)
FGF2	20 ng/mL	100ug/ml
Day 2: Lateral mesoderm	**Final**	**Initial**
BMP4	40 ng/mL	100ug/ml
GDC0941	2.5µM	10mM
VEGF	100 ng/mL	100ug/ml
XAV939	1 µM	10mM
Forskolin	10 µM	10mM
SB505124	2 µM	10mM
AA2P	200 µg/mL	50mg/ml

Day 3; ARTERY meidum		
Activin A	15 ng/mL	50ug/ml
GDC0941	2.5 µM	10mM
VEGF	100 ng/mL	100ug/ml
XAV939	1 µM	10mM
AA2P	200 µg/mL	50mg/ml
DMH1	250nM	1mM

Day 3,4: VEIN medium		
Day 3 Vein medium	**Final**	**Initial**
SB505124	2 µM	10mM
DMH1	250nM	1mM
RO4929097	2 µM	10mM
VEGF	100 ng/mL	100ug/ml
XAV939	1 µM	10mM
AA2P	200 µg/mL	50mg/ml
Day 4 Vein medium	**Final**	**Initial**
SB505124	2 µM	10mM
RO4929097	2 µM	10mM
PD0325901	0.5 µM	5mM
CHIR99021	1 µM	10mM
AA2P	200 µg/mL	50mg/ml

Rescue experiment of vein endothelial cells using R(+) Propranolol and Sm4:

For rescue experiments, NR2F2^{WT} and NR2F2^{c994del} were treated with R(+) propranolol at 15 µM and Sm4 at 30 µM while differentiating cells in a day 4 vein medium, and cells were processed for FACS and qPCR analysis as described in respective sections.

Flow Cytometry

Cells were dissociated by incubation in Accutase for 5 mins at 37ºC. Dissociated cells were diluted 1:5 in DMEM/F12+5% FBS (Thermo Fischer Scientific, # A5670401) and centrifuged at 350g for 5 minutes. Cell pellets were resuspended in FACS buffer (PBS+1mM EDTA+2% FBS+1%

penicillin/Streptomycin). Cells were then blocked for 5 minutes in the presence of an FcR blocking reagent (Miltenyi Biotec, # 130-059-901) followed by staining with PE anti-human CD73 (BioLegend, #344004) and FITC anti-human (BD Biosciences, #560411) for 30 minutes on ice protected from light. Cells were then washed with FACS buffer (1:5), and resuspended in 300µl FACS buffer + DAPI ((Miltenyi Biotec, # 130-111-570) for live/dead cell identification. Cells were then analyzed using a Sony MA900 Multi-application cell sorter. For analysis, cells were gated on forward, and side scatter, followed by height and width parameters for singlet identification. Finally, DAPI negative (live cells) were gated for CD73 and CD144 populations.

ATAC-seq

HUVECs were cultured in medium 199 (Sigma-Aldrich, MO, USA) supplemented with 16% fetal bovine serum (FBS), 100 U/ml penicillin, 100 U/ml streptomycin, 15 µg/ml endothelial cell growth factor (BD Biosciences, MA, USA) and 15 µg/ml heparin (Sigma-Aldrich, MO, USA) at a humidified 37 ◦C, 5% CO2 incubator.

HUVECs were grown to 60% confluence then treated with 25uM Sm4 or the equivalent volume of DMSO. 24hrs after treatment 3 HUVEC lines were harvested and pooled. ATAC-seq and ATAC-seq analysis were performed by Active Motif. As per their sample preparation instructions, 150k cells/sample were collected, centrifuged at 500 x g at 4°C to remove the supernatant. Then resuspended in ice-cold cryopreservation solution (50% FBS, 40% media, and 10% DMSO) and transferred to cryotubes for freezing down. Samples were then shipped to Active Motif for analysis.

HS17 sample preparation

The human embryo samples were collected for pathological examination, which entails histological verification of pregnancy and confirmation of fetal components. In addition, they were assessed to ensure the absence of conditions such as hydatidiform mole or choriocarcinoma. We selected residual specimens, collected between January 2000 and October 2021. The use of human samples was approved by the Ethics Committee of Mie University Hospital (approval number: H2021-228). Informed consent was acquired at the time of surgery, complemented by the availability of an opt-out provision, ensuring participants' autonomy to withdraw from the study at any point. The staging of the embryos and fetuses used in the experiments was done using a combination of the Tissue collection and ethical considerations. For this study, 31 preserved human embryos in organogenesis period and 3 fetuses ranging from CS8 to GW9 were analyzed. The samples were collected for pathological examination, which entails histological verification of pregnancy (investigating the decidua's interstitial and the endometrium's Arias-Stella reactions) and confirmation of fetal components (examination of chorionic tissue). In addition, they were assessed to ensure the absence of conditions such as hydatidiform mole or choriocarcinoma. We selected residual specimens, collected between January 2000 and October 2021, that included embryos and utilized these specimens specifically for the purposes of this research.

Immunohistochemistry (IHC)

Proband samples

Prior to staining the samples were processed to remove paraffin wax through multiple xylene and ethanol baths. Epitope retrieval was performed using Tris-EDTA. To stain the sample sections the samples were submerged in blocking buffer consisting of 1M maleic acid (Sigma, M0375), 10% heat inactivated horse serum (Sigma, H1138), 1% DMSO (Sigma, 472301), 0.1% PBTX (PBS + 0.1% Tween-20) (Tween-20, Sigma, P7949) for 1hr. Antibodies were then diluted into blocking buffer at 1:50 for anti-hCD31 (Abcam, ab28364) and 1:250 for anti-hNR2F2 (R&D systems, PPH714700) and anti-hSOX18 (Santa Cruz Biotechnology, sc-166025) overnight in the dark at 4C. The next day the slides were washed in blocking buffer three times over the course of 30min. Secondary antibodies were diluted in blocking buffer at 1:300 (ThermoFisher (Alexa Fluor 488 goat anti-rabbit IgG, A11008), (Alexa Fluor 555 goat anti-mouse IgG2a, A21137), (Alexa Fluor 647 goat anti-mouse IgG1, A21240))

for 1hr at room temp in the dark. Samples were then washed with PBS three times over 30min. Hoechst (ThermoFisher, R37605)) was diluted in PBS at 1:1000 and added to the slides for 10 min, then washed twice with PBS and mounted. Imaging was performed on a Zeiss 800 LSM. All images were processed using ImageJ software.

HS17 sample

IHC was performed using 3-µm thick sections. The sections were deparaffinised and rehydrated through a series of xylene and ethanol. To suppress autofluorescence, samples were incubated in 0.1% sodium borohydride in 0.1M phosphate-buffered saline (PBS) (137 mM NaCl, 2.7 mM KCl, 10 mM Na2HPO4, and 1.8 mM KH2PO4, pH 7.2) for 30 minutes, rinsed with water, and subsequently incubated for 5 minutes in 0.2M glycine in 0.1M PBS. Antigen retrieval was carried out using a pressure chamber with Tris-EDTA buffer (7.4 mM Tris, 1 mM EDTA-2Na, pH 9.0). Slides were incubated with primary antibodies against Prox1 (AF2727, R&D Systems, 1:150, RRID), Coup-TF2 (EPR18443, Abcam, 1:150, RRID), and SOX18 (sc-166025, Santa Cruz Biotechnology, 1:50, RRID). Alexa Fluor-conjugated secondary antibodies (Abcam, 1:400) were subsequently applied. Imaging was carried out using a Keyence BZ-X700 microscope. All images were processed using ImageJ software.

Immunofluorescent staining of IH, VM and AVM FFPE patient tissue sections

FFPE tissue sections (5 µm) from patients with IH, VM or AVM were deparaffinized, immersed in an antigen retrieval solution (citrate-EDTA buffer containing 10 mM citric acid, 2 mM EDTA, and 0.05% Tween-20, pH 6.2) for 20 minutes at 95°C–99°C, cooled down and washed. Blocked for 30 min was performed in 10% donkey serum followed by incubation overnight at 4C with monoclonal IgG1 mouse anti-human SOX18 (D-8) (1:50, Santa Cruz Biotechnology, sc-166025), monoclonal IgG_{2A} mouse anti-human COUP-TF II (1:100, R&D, PP-H7147-00), and UEA1 fluorescently labeled with Alexa Fluor 649 (1:50, Vector Laboratories, DL1068). Next, the sections were incubated with Alexa Fluor 546 goat anti-mouse IgG1 (1:200; cross-absorbed, Invitrogen, A-21123) and Alexa Fluor 488 goat anti-mouse IgG_{2A} (1:200; cross-absorbed, Invitrogen, A-21137) as secondary antibodies for 45 minutes at room temperature. All slides were mounted using DAPI (Molecular Probes) to visualize nuclei. IF Images were acquired using a LSM 880 confocal microscope (Zeiss) through a 63x objective lens. All images were analyzed using Fiji ImageJ software.

Immunofluorescent cell staining of HemSC, HemEC, and ECFC

Hemangioma stem cells (HemSC), hemangioma endothelial cells (HemEC) and endothelial colony forming cells (ECFC) were seeded on fibronectin-coated plates at a density of 30,000 cells/cm^2 in EGM-2 media for 30 hours on 2 cm^2 slides, fixed in 4% PFA and blocked in 5% BSA/0.3% Triton x-100 for 1 hour. Cells were co-stained for monoclonal IgG1 mouse anti-human SOX18 (D-8) (1:100, Santa Cruz Biotechnology, sc-166025), monoclonal IgG_{2A} mouse anti-human COUP-TF II (1:200, R&D, PP-H7147-00). Alexa Fluor 546 goat anti-mouse IgG1 (1:200; cross-absorbed, Invitrogen, A-21123) and Alexa Fluor 488 goat anti-mouse IgG_{2A} (1:200; cross-absorbed, Invitrogen, A-21137) served as secondary antibodies, incubation was for 45 minutes at room temperature. DAPI was used to visualize nuclei (Molecular Probes) followed by mounting (Invitrogen). Immunostainings of IH sections with respective isotype matched control IgG and secondary antibodies were conducted.

RNA isolation and RT-qPCR

hESC

Total RNA was exracted using Trizol reagent (ThermoFisher Scientific, #1559608). RNA concentration was determined using Nanodrop (Thermoscientific). cDNA was produced using verso cDNA synthesis kit (ThermoFisher Scientific, #1453B). qPCR amplification was performed using PowerUP SYBR

Green (ThermoFischer Scientific, #A25778) on a Quantstudio 7 Flex (ThermoFischer Scientific). The $2^{-\Delta\Delta CT}$ method was used to calculate relative gene expression relative to YWHAZ.

HUVEC drug treatment

The day before collection 300k cells/well were seeded in a 6 well plate. The following day HUVECs were treated with either CIA1 (Tocris, 7494) at 4µM or CIA1 at 4µM + R(+)propranolol (Sigma, P0689) at 25µM for 4 hours prior to collection. After 4 hours cells were washed with PBS. RNA was extracted using Trizol reagent (ThermoFisher, #1559618). RNA concentration was determined using Nanodrop (Thermo Scientific). cDNA was produced using cDNA kit (Bio-Rad, 1725035) and qPCR amplification was performed using SensiFAST SYBR kit (Bio-Rad, BIO-98050) on a Roche Lightcycler 480 II. The $2^{-\Delta\Delta CT}$ method was used to calculate relative gene expression relative to GAPDH.

IH cells

Total RNA was extracted from cells with the RNeasy Micro Extraction Kit (QIAGEN). Reverse transcriptase reactions were performed using an iScript cDNA Synthesis Kit (Bio-Rad). qPCR was performed using SYBR FAST ABI Prism 2× qPCR Master Mix (Kapa BioSystems). Amplification was carried out in a QuantStudio 6 Flex Real-Time PCR System (Fisher Scientific). A relative standard curve for each gene amplification was generated to determine the amplification efficiency, with greater than 90% considered acceptable. Fold increases in gene expression were calculated according to the ΔΔCt method, with each amplification reaction performed in duplicate or triplicate. ATP5B was used as housekeeping gene expression reference. A list of all primer sequences used in this study is attached below.

Primers

Gene	Seq (5'-3')	Seq (3'-5')
APLNR	CTCTGGACCGTGTTTCGGAG	GGTACGTGTAGGTAGCCCACA
ATP5B	CCACTACCAAGAAGGGATCTATCA	GGGCAGGGTCAGTCAAGTC
CD144	AACGAGCAGGGCGAGTTCACCTTC	TAGGTGACCAGCTGCTCGTGGATC
CD31	CACCTGGCCCAGGAGTTTC	AGTACACAGCCTTGTTGCCATGT
DCBLD2	CTGAGAGTGGAACCCTTACA	CGAACTCTCTCTCCCATCTT
DIAPH3	GGACACTGACGGATGATATG	GTCTTCAGGTTGGGAAGTG
EPHB4	AGAGGCCGTACTGGGACATGAG	TCCAGCATGAGCTGGTGGAG
FAM171A1	ACGCTCTGCCACTCTAAT	GCCCTTCTCTGGAAATGAAC
GALNT1	CTAGCCACCTCCTTGATTTG	CAGGAAGTCCTCTCTCCTTT
GAPDH	CCCCGGTTTCTATAAATTGAGC	CACCTTCCCCATGGTGTCT
LMO7	AGGCCCTCCAAACATACT	GATTCTTCCTGCGGGTTATG
MBNL1	GGTACTAAGAAGTGCCTTTCC	TGCTGTCGTCACAGTCTA
NR2F2	CCATAGTCCTGTTCACCTCAGA	AATCTCGTCGGCTGGTTG
NRP2	GCTGGCTATATCACCTCTCCC	TCTCGATTTCAAAGTGAGGGTTG
NT5E	CCAGTACCAGGGCACTATCTG	TGGCTCGATCAGTCCTTCCA
SLC26A4	GACGTCATTTCGGGAGTTAG	AGCAGAGTAGAGACCATATCC
SLC45A1	CCATCCTCGGATTCCTACT	CCCTATAGCCAGGACAAGA
SOX17	CAGAATCCAGACCTGCACAA	GCGGCCGGTACTTGTAGTT
SOX18	AAGCGTGGAAGGAGCTGAAC	CGCGGCCGGTACTTGTAGTT
SOX7	TCGACGCCCTGGATCAACT	CTGGGAGACCGGAACATGC

THBS1	CAACTCTCACAGCGACATT	CCTCCCTCATCCACATTTAC
YWHAZ	ACCGTTACTTGGCTGAGGTTGC	CCCAGTCTGATAGGATGTGTTGG

NR2F2^{c994del} Plasmid creation

Halo-NR2F2^{WT} (Genecopoeia, EX-C0221-M49) was used as a template to construct the c994del variant plasmid using the megaprimer sight-directed mutagenesis method. The Halo-NR2F2^{c994del} plasmid was validated by sanger sequencing to ensure the deletion occurred at position at 994.

Quantitative molecular imaging

Single-molecule tracking (SMT)

SMT Sample preparation

Single-molecule tracking was performed as described in McCann et al.[23]. HeLa cells were seeded at a density of 23,000 cells/well in 8-well chamber glass slides (Ibidi, 80827) coated with 0.5% gelatine 24h prior to transfection. 300ng of plasmid DNA/well of either Halo-tagged NR2F2^{WT} or NR2F2^{c994del} was transiently transfected into the cells using X-tremeGENE 9 Transfection Reagent kit (Roche, XTG9RO). For dual transfection experiments 600ng (300ng of each plasmid) of plasmid DNA/well of Halo-tagged NR2F2^{WT} + eGFP-SOX18, NR2F2^{c994del} + eGFP-SOX18, Halo-tagged SOX18 + eGFP-NR2F2^{WT}, or SOX18 + eGFP-NR2F2^{c994del}. Cells were then incubated at 37°C with 5% CO_2 overnight prior to imaging then washed three times and then incubated in imaging media (Fluorobrite DMEM (Glibco), 10% FBS, 1% HEPES, 1% GlutaMax) 45 min prior to imaging 1nM of JF549 Halo-tag ligand (Promega, GA1111) was added directly to the media and cells were incubated for 10 minutes at 37 ° C with 5% of CO_2. Following incubation, cells were washed twice 15min apart and replaced with imaging media.

SMT acquisition

Images were acquired on a Nikon TIRF microscope at a TIRF angle of 61 degrees to achieve HILO illumination. Samples were recorded with an iXon Ultra 888 EMCCD camera, filter cube TRF49909 – ET – 561 laser bandpass filter and 100 X oil 1.49 NA TIRF objective. Cells were imaged using a 561nm excitation laser at a power density of 10.3 µW to perform two different acquisition techniques. A fast frame rate which uses a 50 Hz (20ms acquisition speed) to acquire 6000 frames without intervals to measure displacement distribution and fraction bound, and a slow frame rate which uses a 2 Hz (500ms acquisition speed) to acquire 500 frames without intervals to measure residence times.

SMT analysis

Masking and segmentation of the nucleus was performed in ImageJ for all files. To identify and track molecules a custom-written MATLAB implementation of the multiple target tracing (MTT) algorithm, known as SLIMfast was used[77]. Parameters used for fast frame rate analysis: Localization error: $10^{-6.5}$, blinking (frames) = 1, max # of competitors: 3, max expected diffusion coefficient = 3µm^2/sec, box size = 7, timepoints = 7, clip factor = 4. Cells with less than 500 trajectories based on the above parameters were excluded from analysis. The first four frames of each trajectory were used to calculate the mean squared displacement. Diffusion coefficient was calculated from each trajectory's mean squared displacement and plotted. An inflection point was determined on WT NR2F2 diffusion profile and used as a boundary to determine confined vs non-confined states for all conditions. The confined fraction and non-confined fraction of each cell were calculated by computing the number of trajectories whose mean diffusion coefficient were defined as confined and non-confined respectively. Parameters used for slow frame rate analysis: Localization error: 10^{-7}, blinking (frames): 1, max # of competitors: 3, max expected diffusion coefficient = 0.33µm^2/sec, box size = 9. Slow-tracking analysis was performed using custom MATLAB code based on [52].

Fluorescence fluctuation spectroscopy (FFS)

Halo Tag labelling for FFS experiment

To saturate all Halo Tags with Janelia Farm dyes 549 or 646 for single or dual-color labelling, HeLa cells transiently expressing Halo Tag-tagged Sox7, NR2F2 or NR2F2_C994del constructs were incubated with a saturating concentration of a single JF dye (JF549, 100 nM) or two JF dyes (JF549 : JF646, 100 nM : 100 nM) for 15 minutes at 37 °C, similar to McCann et al.[23]. Cells were washed twice with 1× PBS before imaging experiments.

FFS acquisition

All FFS measurements for Number and Brightness (NB) analysis and cross Raster Image Correlation Spectroscopy (RICS) were performed on an Olympus FV3000 laser scanning microscope coupled to an ISS A320 Fast FLIM box for fluorescence fluctuation data acquisition. For single channel NB FFS measurements, HaloJF549 tagged plasmids were excited by a solid-state laser diode operating at 561 nm and the resulting fluorescence signal was directed through a 405/488/561 dichroic mirror to an external photomultiplier detector (H7422P-40 of Hamamatsu) fitted with a mCherry 600-640 nm bandwidth filter. For dual channel RICS FFS measurements (that enable cross RICS), the HaloJF546 and HaloJF646 combination were excited by solid-state laser diodes operating at 561 nm and 640 nm, respectively, and the resulting signal was directed through a 405/488/561/640 dichroic mirror to two internal GaAsP photomultiplier detectors set to collect 600-640 nm and 650-750 nm, respectively.
All FFS data acquisitions (i.e., NB, cross RICS) employed a 60X water immersion objective (1.2 NA) and first involved selecting a 10.6 µm region of interest (ROI) within a HeLa cell nucleus at 37 °C in 5% CO2 that exhibited low protein expression level (nanomolar) to ensure observation of fluctuations in fluorescence intensity[78]. Then a single or simultaneous two channel frame scan acquisition was acquired (N = 100 frames) in the selected ROI with a pixel frame size of 256 x 256 (i.e., pixel size ~ 41nm) and a pixel dwell time of 12.5 µs. These conditions resulted in scanning pattern that was found to be optimal for simultaneous capture of the apparent brightness and mobility of the Halo tagged constructs being characterised by NB and cross RICS analysis; all of which was performed in the SimFCS software developed at the Laboratory for Fluorescence Dynamics (LFD).

Number and brightness (NB) analysis

The oligomeric state of the different HaloJF549-tagged plasmids investigated was extracted and spatially mapped throughout single channel FFS measurements via a moment-based brightness analysis that has been described in previously published papers [79,80]. In brief, within each pixel of an NB FFS measurement there is an intensity fluctuation F(t) which has: (1) an average intensity $\langle F(t) \rangle$ (first moment) and (2) variance σ^2 (second moment); and the ratio of these two properties describes the apparent brightness (B) of the molecules that give rise to the intensity fluctuation. The true molecular brightness (ε) of the fluorescent molecules being measured is related to B by $B = \varepsilon + 1$, where 1 is the brightness contribution of a photon counting detector. Thus, if we measure the B of monomeric HaloJF549-Sox7 ($B_{monomer} = \varepsilon_{monomer} + 1$) under our NB FFS measurement conditions, then we can determine $\varepsilon_{monomer}$ and extrapolate the expected B of HaloJF549-tagged dimers ($B_{dimer} = (2 \times \varepsilon_{monomer}) + 1$) or oligomers (e.g., $B_{tetramer} = (4 \times \varepsilon_{monomer}) + 1$), *and in turn define* brightness cursors, to extract and spatially map the fraction of pixels within a NB FFS measurement that contain these different species. These cursors were used to extract the fraction of HaloJF549-NR2F2 dimer and oligomer (i.e., number of pixels assigned B_{dimer} or $B_{oligomer}$) within a NB FFS measurement and quantify the degree of NR2F2 self-association across multiple cells. Artefact due to cell movement or photobleaching were subtracted from acquired intensity fluctuations via use of a moving average algorithm and all brightness analysis was carried out in SimFCS from the Laboratory for Fluorescence Dynamics.

Cross RICS analysis

The fraction of interaction between the HaloJF549 and HaloJF646-tagged NR2F2 or NR2F2-C994del plasmids was extracted via application of cross RICS functions described in previously published papers to the dual channel FFS measurements[23,78]. In brief, the fluorescence intensity recorded within each frame (N =100) of each channel (i.e., CH1 and CH2) was spatially correlated via application of the RICS function, and spatially cross-correlated between channels (CC) via application of the cross RICS function, alongside a moving average algorithm (N = 10 frames) in both instances. Then the

recovered RICS and cross RICS correlation profiles were fit to a 3D diffusion model and the amplitude versus decay of each fit recorded in the form of a G value and diffusion coefficient (D) respectively. The ratio of the cross RICS amplitude (i.e., G_{CC}) with the limiting channel RICS amplitude (i.e., G_{CH1} or G_{CH2}) enabled the fraction of HaloJF549-NR2F2 molecules interacting with Halo646-NR2F2 molecules to be extracted. All cross RICS analysis was carried out in SimFCS from the Laboratory for Fluorescence Dynamics.

Statistics

All statistical analysis was performed on GraphPad Prism. An outlier test using settings (Q=1) was performed to identify and remove outliers. Results are displayed as mean ± the standard deviation unless indicated otherwise.

Study approvals and ethics

Proband samples The use of the proband's samples was approved by the Hunter New England Exemption from HREC case study (authorization number: AU2206-11) and the Hunter New England Human Research Ethics Committee (2023/PID0317). All procedures were conducted in compliance with guidelines and regulations. ***hESCs*** The use of human embryonic stem cells (hESCs) in this study was approved by Stem Cell Research Oversight (SCRO) at Stanford University. All procedures were conducted in compliance with institutional guidelines and regulations. ***CS17 sample*** The use of human samples was approved by the Ethics Committee of Mie University Hospital (approval number: H2021-228). Informed consent was acquired at the time of surgery, complemented by the availability of an opt-out provision, ensuring participants' autonomy to withdraw from the study at any point. ***HemSC, HemEC, and ECFC*** Vascular anomaly specimens were obtained under protocols approved by the Committee on Clinical Investigation at Boston Children's Hospital (IRB protocol number 04-12-175R and P00003505; AH, JB). Patient specimens were collected upon written informed consent of the patient or the patient's guardian, de-identified, and used for cell isolation as well as tissue staining under a Boston Children's Hospital IRB approved protocol (04-12-175R and P00003505) and in accordance with Declaration of Helsinki principles. ***HUVEC cells*** Umbilical cords were collected from the Royal Prince Alfred Hospital upon written informed consent of the patient or the patient's guardian, de-identified, and used for cell isolation of human umbilical vein endothelial cells (HUVECs). Isolation protocol was as previously described in Litwin et al.[81] and cells were used from passage 1 to 3. Ethics approval for the collection of the umbilical cords was from SLHD Protocol No. X16-0225.

References:

1. Eifert, S., Villavicencio, J. L., Kao, T.-C., Taute, B. M. & Rich, N. M. Prevalence of deep venous anomalies in congenital vascular malformations of venous predominance. *Journal of Vascular Surgery* **31**, 462–471 (2000).
2. Tasnádi, G. Epidemiology of Vascular Malformations. in *Hemangiomas and Vascular Malformations: An Atlas of Diagnosis and Treatment* (eds. Mattassi, R., Loose, D. A. & Vaghi, M.) 109–110 (Springer Milan, Milano, 2009). doi:10.1007/978-88-470-0569-3_14.
3. Fu, X. & Rabadan, R. Understanding variants of unknown significance: the computational frontier. *The Oncologist* **29**, 653–657 (2024).
4. Zaidi, S. & Brueckner, M. Genetics and Genomics of Congenital Heart Disease. *Circ Res* **120**, 923–940 (2017).
5. You, L.-R. *et al.* Suppression of Notch signalling by the COUP-TFII transcription factor regulates vein identity. *Nature* **435**, 98–104 (2005).
6. McCracken, I. R., Baker, A. H., Smart, N. & De Val, S. Transcriptional regulators of arterial and venous identity in the developing mammalian embryo. *Current Opinion in Physiology* **35**, 100691 (2023).
7. Swift, M. R. *et al.* SoxF factors and Notch regulate *nr2f2* gene expression during venous differentiation in zebrafish. *Developmental Biology* **390**, 116–125 (2014).
8. Aranguren, X. L. *et al.* COUP-TFII orchestrates venous and lymphatic endothelial identity by homo- or hetero-dimerisation with PROX1. *Journal of Cell Science* **126**, 1164–1175 (2013).
9. Aranguren, X. L. *et al.* Transcription factor COUP-TFII is indispensable for venous and lymphatic development in zebrafish and *Xenopus laevis*. *Biochemical and Biophysical Research Communications* **410**, 121–126 (2011).
10. Lin, F.-J. *et al.* Endocardial Cushion Morphogenesis and Coronary Vessel Development Require Chicken Ovalbumin Upstream Promoter-Transcription Factor II. *Arterioscler Thromb Vasc Biol* **32**, e135–e146 (2012).

842 11. Pereira, F. A., Qiu, Y., Zhou, G., Tsai, M.-J. & Tsai, S. Y. The orphan nuclear receptor COUP-TFII is
843 required for angiogenesis and heart development. *Genes Dev* **13**, 1037–1049 (1999).
844 12. Su, T. *et al.* Single-cell analysis of early progenitor cells that build coronary arteries. *Nature* **559**,
845 356–362 (2018).
846 13. Wang, J. *et al.* NR2F2 loss-of-function mutation is responsible for congenital bicuspid aortic
847 valve. *International Journal of Molecular Medicine* **43**, 1839–1846 (2019).
848 14. Qiao, X.-H. *et al.* A novel NR2F2 loss-of-function mutation predisposes to congenital heart
849 defect. *European Journal of Medical Genetics* **61**, 197–203 (2018).
850 15. Al Turki, S. *et al.* Rare Variants in NR2F2 Cause Congenital Heart Defects in Humans. *Am J Hum*
851 *Genet* **94**, 574–585 (2014).
852 16. High, F. A. *et al.* De novo frameshift mutation in COUP-TFII (NR2F2) in human congenital
853 diaphragmatic hernia. *American Journal of Medical Genetics Part A* **170**, 2457–2461 (2016).
854 17. Bashamboo, A. *et al.* Loss of Function of the Nuclear Receptor NR2F2, Encoding COUP-TF2,
855 Causes Testis Development and Cardiac Defects in 46,XX Children. *The American Journal of*
856 *Human Genetics* **102**, 487–493 (2018).
857 18. Chen, X., Qin, J., Cheng, C.-M., Tsai, M.-J. & Tsai, S. Y. COUP-TFII Is a Major Regulator of Cell
858 Cycle and Notch Signaling Pathways. *Molecular Endocrinology* **26**, 1268–1277 (2012).
859 19. Sissaoui, S. *et al.* Genomic Characterization of Endothelial Enhancers Reveals a Multifunctional
860 Role for NR2F2 in Regulation of Arteriovenous Gene Expression. *Circulation Research* **126**, 875–
861 888 (2020).
862 20. Kumarasamy, S. *et al.* Mutation within the hinge region of the transcription factor Nr2f2
863 attenuates salt-sensitive hypertension. *Nat Commun* **6**, 6252 (2015).
864 21. Dinh, T. T. *et al.* An NKX-COUP-TFII morphogenetic code directs mucosal endothelial addressin
865 expression. *Nat Commun* **13**, 7448 (2022).
866 22. Overman, J. *et al.* Pharmacological targeting of the transcription factor SOX18 delays breast
867 cancer in mice. *eLife* **6**, e21221.

868 23. McCann, A. J. *et al.* A dominant-negative SOX18 mutant disrupts multiple regulatory layers
869 essential to transcription factor activity. *Nucleic Acids Res* **49**, 10931–10955 (2021).
870 24. Srinivasan, R. S. *et al.* The nuclear hormone receptor Coup-TFII is required for the initiation and
871 early maintenance of Prox1 expression in lymphatic endothelial cells. *Genes Dev.* **24**, 696–707
872 (2010).
873 25. Duong, T. *et al.* VEGFD regulates blood vascular development by modulating SOX18 activity.
874 *Blood* **123**, 1102–1112 (2014).
875 26. Fontijn, R. D. *et al.* SOX-18 controls endothelial-specific claudin-5 gene expression and barrier
876 function. *American Journal of Physiology-Heart and Circulatory Physiology* **294**, H891–H900
877 (2008).
878 27. Garcia-Flores, A. E. *et al.* Loss of SOX18/CLAUDIN5 disrupts the pulmonary endothelial barrier in
879 ventilator-induced lung injury. *Front Physiol* **13**, 1066515 (2022).
880 28. François, M. *et al.* Sox18 induces development of the lymphatic vasculature in mice. *Nature* **456**,
881 643–647 (2008).
882 29. Patel, J. *et al.* Functional Definition of Progenitors Versus Mature Endothelial Cells Reveals Key
883 SoxF-Dependent Differentiation Process. *Circulation* **135**, 786–805 (2017).
884 30. Donovan, P. *et al.* Endovascular progenitors infiltrate melanomas and differentiate towards a
885 variety of vascular beds promoting tumor metastasis. *Nat Commun* **10**, 18 (2019).
886 31. Duong, T. *et al.* Genetic Ablation of SOX18 Function Suppresses Tumor Lymphangiogenesis and
887 Metastasis of Melanoma in Mice. *Cancer Research* **72**, 3105–3114 (2012).
888 32. Moalem, S. *et al.* Hypotrichosis-lymphedema-telangiectasia-renal defect associated with a
889 truncating mutation in the SOX18 gene. *Clin Genet* **87**, 378–382 (2015).
890 33. Dailey, C., Oshodi, R. B., Boull, C. & Aggarwal, A. Expanding the clinical spectrum of *SOX18*-
891 related Hypotrichosis-lymphedema-telangiectasia-renal defect syndrome. *European Journal of*
892 *Medical Genetics* **65**, 104607 (2022).

893 34. Chen, J. *et al.* SOX18 promotes gastric cancer metastasis through transactivating MCAM and
894 CCL7. *Oncogene* **39**, 5536–5552 (2020).
895 35. Seebauer, C. T. *et al.* Non–beta blocker enantiomers of propranolol and atenolol inhibit
896 vasculogenesis in infantile hemangioma. *J Clin Invest* **132**, (2022).
897 36. Overman, J. *et al.* R-propranolol is a small molecule inhibitor of the SOX18 transcription factor in
898 a rare vascular syndrome and hemangioma. *Elife* **8**, e43026 (2019).
899 37. Fontaine, F. *et al.* Small-Molecule Inhibitors of the SOX18 Transcription Factor. *Cell Chemical*
900 *Biology* **24**, 346–359 (2017).
901 38. Holm, A. *et al.* An endothelial SOX18-mevalonate pathway axis enables repurposing of statins
902 for infantile hemangioma. *J Clin Invest* (2025) doi:10.1172/JCI179782.
903 39. Jumper, J. *et al.* Highly accurate protein structure prediction with AlphaFold. *Nature* **596**, 583–
904 589 (2021).
905 40. Cheng, J. *et al.* Accurate proteome-wide missense variant effect prediction with AlphaMissense.
906 *Science* (2023) doi:10.1126/science.adg7492.
907 41. Kruse, S. W. *et al.* Identification of COUP-TFII Orphan Nuclear Receptor as a Retinoic Acid–
908 Activated Receptor. *PLOS Biology* **6**, e227 (2008).
909 42. Bryant, P., Pozzati, G. & Elofsson, A. Improved prediction of protein-protein interactions using
910 AlphaFold2. *Nat Commun* **13**, 1265 (2022).
911 43. Mirdita, M. *et al.* ColabFold: making protein folding accessible to all. *Nat Methods* **19**, 679–682
912 (2022).
913 44. Calvo, K. R. & Hickstein, D. D. The spectrum of GATA2 deficiency syndrome. *Blood* **141**, 1524–
914 1532 (2023).
915 45. Mellor, R. H. *et al.* Mutations in FOXC2 Are Strongly Associated With Primary Valve Failure in
916 Veins of the Lower Limb. *Circulation* **115**, 1912–1920 (2007).

917 46. Irrthum, A. *et al.* Mutations in the Transcription Factor Gene SOX18 Underlie Recessive and
918 Dominant Forms of Hypotrichosis-Lymphedema-Telangiectasia. *Am J Hum Genet* **72**, 1470–1478
919 (2003).
920 47. Valenzuela, I. *et al.* Further delineation of the *SOX18*-related Hypotrichosis, Lymphedema,
921 Telangiectasia syndrome (HTLS). *European Journal of Medical Genetics* **61**, 269–272 (2018).
922 48. Ang, L. T. *et al.* Generating human artery and vein cells from pluripotent stem cells highlights the
923 arterial tropism of Nipah and Hendra viruses. *Cell* **185**, 2523-2541.e30 (2022).
924 49. Digman, M. A. & Gratton, E. Lessons in Fluctuation Correlation Spectroscopy. *Annu Rev Phys*
925 *Chem* **62**, 645–668 (2011).
926 50. Digman, M. A., Dalal, R., Horwitz, A. F. & Gratton, E. Mapping the Number of Molecules and
927 Brightness in the Laser Scanning Microscope. *Biophys J* **94**, 2320–2332 (2008).
928 51. Hinde, E. *et al.* Quantifying the dynamics of the oligomeric transcription factor STAT3 by pair
929 correlation of molecular brightness. *Nat Commun* **7**, 11047 (2016).
930 52. Chen, J. *et al.* Single-Molecule Dynamics of Enhanceosome Assembly in Embryonic Stem Cells.
931 *Cell* **156**, 1274–1285 (2014).
932 53. Ibarra-Soria, X. *et al.* Defining murine organogenesis at single-cell resolution reveals a role for
933 the leukotriene pathway in regulating blood progenitor formation. *Nat Cell Biol* **20**, 127–134
934 (2018).
935 54. Dunham, I. *et al.* An integrated encyclopedia of DNA elements in the human genome. *Nature*
936 **489**, 57–74 (2012).
937 55. McLean, C. Y. *et al.* GREAT improves functional interpretation of cis-regulatory regions. *Nat*
938 *Biotechnol* **28**, 495–501 (2010).
939 56. Tanigawa, Y., Dyer, E. S. & Bejerano, G. WhichTF is functionally important in your open
940 chromatin data? *PLOS Computational Biology* **18**, e1010378 (2022).
941 57. Wang, L. *et al.* Small-molecule inhibitor targeting orphan nuclear receptor COUP-TFII for
942 prostate cancer treatment. *Science Advances* **6**, eaaz8031 (2020).

943 58. Schrenk, S. & Boscolo, E. A transcription factor is the target of propranolol treatment in infantile
944 hemangioma. https://www.jci.org/articles/view/156863/pdf (2022) doi:10.1172/JCI156863.
945 59. Gramolelli, S. *et al.* Oncogenic Herpesvirus Engages Endothelial Transcription Factors SOX18 and
946 PROX1 to Increase Viral Genome Copies and Virus Production. *Cancer Res* **80**, 3116–3129 (2020).
947 60. Tuohinto, K. *et al.* KSHV infection of endothelial precursor cells with lymphatic characteristics as
948 a novel model for translational Kaposi's sarcoma studies. *PLoS Pathog* **19**, e1010753 (2023).
949 61. Henley, M. J. & Koehler, A. N. Advances in targeting 'undruggable' transcription factors with
950 small molecules. *Nat Rev Drug Discov* **20**, 669–688 (2021).
951 62. McSwiggen, D. T. *et al.* A high-throughput platform for single-molecule tracking identifies drug
952 interaction and cellular mechanisms. *eLife* **12**, RP93183 (2025).
953 63. Watanabe, D., Hiroshima, M., Yasui, M. & Ueda, M. Single molecule tracking based drug
954 screening. *Nat Commun* **15**, 8975 (2024).
955 64. Shibuya, M. Vascular Endothelial Growth Factor (VEGF) and Its Receptor (VEGFR) Signaling in
956 Angiogenesis. *Genes Cancer* **2**, 1097–1105 (2011).
957 65. Nie, L. *et al.* Transmembrane protein ESDN promotes endothelial VEGF signaling and regulates
958 angiogenesis. *J Clin Invest* **123**, 5082–5097 (2013).
959 66. Alhamoudi, K. M. *et al.* A homozygous nonsense mutation in DCBLD2 is a candidate cause of
960 developmental delay, dysmorphic features and restrictive cardiomyopathy. *Sci Rep* **11**, 12861
961 (2021).
962 67. Marziano, C., Genet, G. & Hirschi, K. K. Vascular endothelial cell specification in health and
963 disease. *Angiogenesis* **24**, 213–236 (2021).
964 68. Krebs, L. T. *et al.* Haploinsufficient lethality and formation of arteriovenous malformations in
965 Notch pathway mutants. *Genes Dev* **18**, 2469–2473 (2004).
966 69. Lin, Y. *et al.* Role of endothelial PDGFB in arterio-venous malformations pathogenesis.
967 *Angiogenesis* **27**, 193–209 (2024).

968 70. Chiang, I. K.-N. *et al.* SoxF factors induce Notch1 expression via direct transcriptional regulation
969 during early arterial development. *Development* **144**, 2629–2639 (2017).
970 71. Sacilotto, N. *et al.* Analysis of Dll4 regulation reveals a combinatorial role for Sox and Notch in
971 arterial development. *Proc Natl Acad Sci U S A* **110**, 11893–11898 (2013).
972 72. Coelho-Santos, V. & Shih, A. Y. Postnatal development of cerebrovascular structure and the
973 neurogliovascular unit. *WIREs Developmental Biology* **9**, e363 (2020).
974 73. Hammill, A. M. *et al.* Sirolimus for the treatment of complicated vascular anomalies in children.
975 *Pediatric Blood & Cancer* **57**, 1018–1024 (2011).
976 74. Seront, E. *et al.* Preliminary results of the European multicentric phase III trial regarding
977 sirolimus in slow-flow vascular malformations. *JCI Insight* **8**, e173095.
978 75. Geeurickx, M. & Labarque, V. A narrative review of the role of sirolimus in the treatment of
979 congenital vascular malformations. *Journal of Vascular Surgery: Venous and Lymphatic Disorders*
980 **9**, 1321–1333 (2021).
981 76. Loh, K. M. *et al.* Protocol for efficient generation of human artery and vein endothelial cells from
982 pluripotent stem cells. *STAR Protocols* **6**, 103494 (2025).
983 77. Sergé, A., Bertaux, N., Rigneault, H. & Marguet, D. Dynamic multiple-target tracing to probe
984 spatiotemporal cartography of cell membranes. *Nat Methods* **5**, 687–694 (2008).
985 78. Lou, J. *et al.* Heterochromatin protein 1 alpha (HP1α) undergoes a monomer to dimer transition
986 that opens and compacts live cell genome architecture. *Nucleic Acids Res* **52**, 10918–10933
987 (2024).
988 79. Hinde, E., Cardarelli, F. & Gratton, E. Spatiotemporal regulation of Heterochromatin Protein 1-
989 alpha oligomerization and dynamics in live cells. *Sci Rep* **5**, 12001 (2015).
990 80. Lou, J., Priest, D. G., Solano, A., Kerjouan, A. & Hinde, E. Spatiotemporal dynamics of 53BP1
991 dimer recruitment to a DNA double strand break. *Nat Commun* **11**, 5776 (2020).

81. Litwin, M. *et al.* Novel Cytokine-independent Induction of Endothelial Adhesion Molecules Regulated by Platelet/Endothelial Cell Adhesion Molecule (CD31). *J Cell Biol* **139**, 219–228 (1997).

Acknowledgments

We thank the Vascular Anomalies Center and Department of Pathology at Boston's Children's Hospital for patient specimens. We acknowledge the technical and scientific staff of Sydney Microscopy & Microanalysis, the University of Sydney node of Microscopy Australia. Research reported in this manuscript was supported by NIH-R01HL12850307 (SJ), University of Sydney Drug Discovery Initiative - seed funding (grant ID: 23059) (MG, PC), Australian Excellence in Diversity Fellowship (JQ), the Vascular Anomalies Center at Boston Children's Hospital (AH), and the Grants-in-Aid for Scientific Research from the Ministry of Education, Culture, Sports, Science, and Technology of Japan (23K15949) and Japan Agency for Medical Research and Development (AMED) (22jm0610079h0001) (KM). KRH was supported by NIH-R01HL12850307 and the Howard Hughes Medical Institute. NHMRC Idea Grants (APP2019904 and APP2029719) (MF)

Author contributions

MG, SJ, MF, and KRH designed the study. MF coordinated the studies with all laboratories and provided the original idea of pharmacological rescue. GM coordinated the interaction between SK and MF. MG, SJ, JQ, AH, PC, TK, WL, and KM conducted experiments. MG, SJ, JQ, AH, YW, and KM carried out formal analysis. AH, SN, ES, TD, and KM provided samples, clinical management, and ethics. MG, AH, TD, EH, and KM performed data curation. MG and MF wrote the original manuscript. All authors reviewed, edited, and agreed to the final version of the manuscript. MF and KRH acquired funding.

Conflict-of-interest statement

MF is on the scientific advisory board of Gertrude Biomedical Pty Ltd., and a shareholder of the company. TK is the CEO of Gertrude Biomedical Pty Ltd. All other authors declare no competing interests.

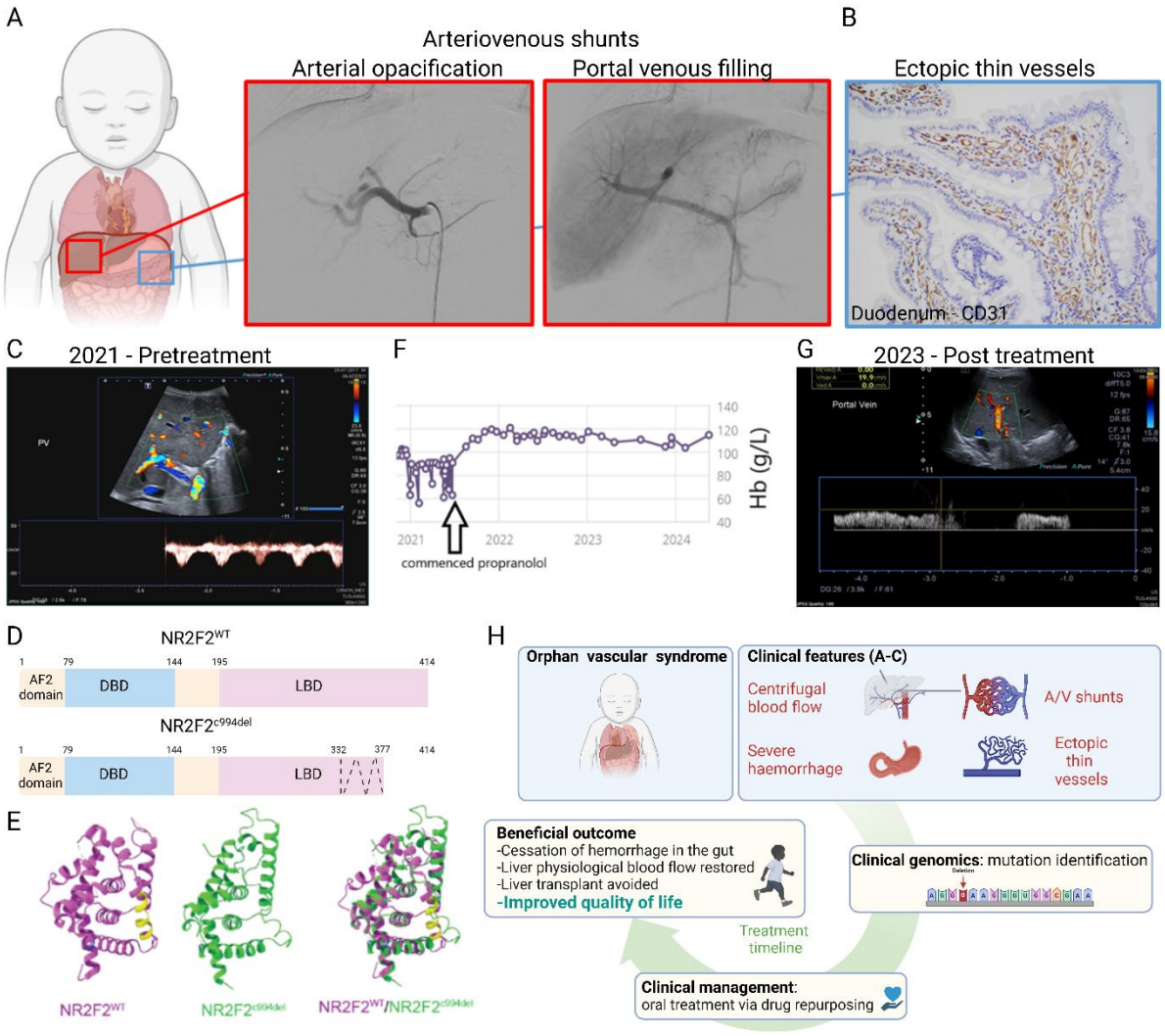

Fig 1: Clinical genetics identifies and characterizes a novel vascular anomaly. A Images from the proband's hepatic angiography. Arterial opacification (left image) and subsequent portal venous filling (right image) showing diffuse arterioportal shunting. **B** Tissue section of duodenum (H&E and counter-stained for CD31), reveals an increased number of thin-walled ectopic vessels. **C** Doppler ultra-sound of the portal vein prior to propranolol treatment shows hepatofugal (reversed) flow in the portal vein consistent with portal hypertension. **D** Schematic representation of $NR2F2^{WT}$ and $NR2F2^{c994del}$. **E** Modeled structure of the LBD of $NR2F2^{WT}$ (purple) and $NR2F2^{c994del}$ (green). The crystal structure of the LBD was previously produced by Kruse et al. This comparison uncovers conformation difference (yellow). **F** Clinical tracking of hemoglobin levels prior and post propranolol treatment. **G** Doppler ultra-sound of portal vein post propranolol treatment showing restoration of physiological blood flow (hepatopetal). **H** Treatment and recovery timeline; including identification of clinical features, identification of NR2F2 variant, followed by propranolol treatment and successful pharmacological management of the condition.

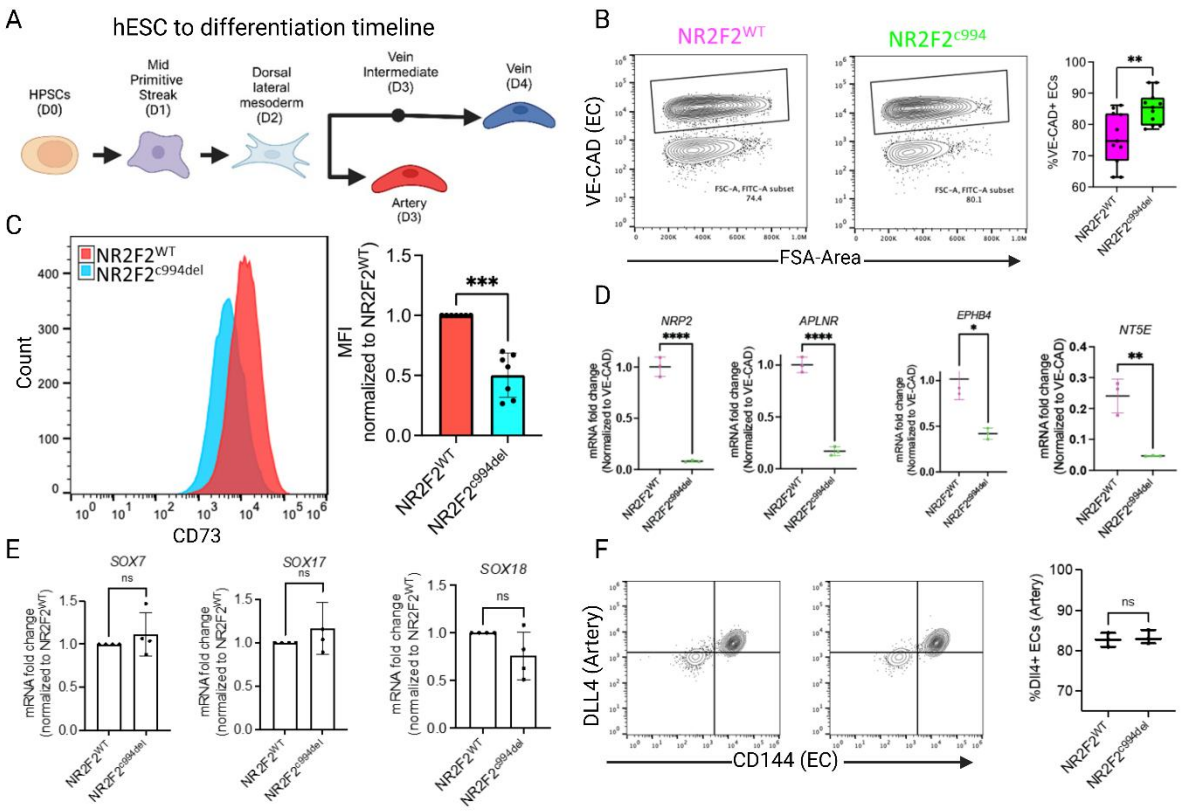

Fig 2: NR2F2^{c994del} impairs differentiation of hESC to venous endothelial cells. A Representative timeline of hESC to EC timeline. **B** Flow cytometry analysis of VE-Cadherin (pan-EC) positive ECs at day 4. WT (purple) c994del (green), Quantification of VE-Cadherin. **C** Histogram plots of CD73 expression in day 4 venous ECs derived from NR2F2^{WT} and NR2F2^{c994del} H1-hESC and corresponding quantification of median fluorescence intensity (MFI). **D,E** qPCR performed on day 4 venous ECs. **F** Flow cytometry analysis of artery ECs at day 4 and corresponding quantification of % DLL4+ CD144+ endothelial cells. Each data point represents independent repeats of n≥3. Statistical significance was determined by Welch's T-test, * $p < 0.05$, ** $p < 0.005$, *** $p < 0.0005$, **** $p < 0.0001$.

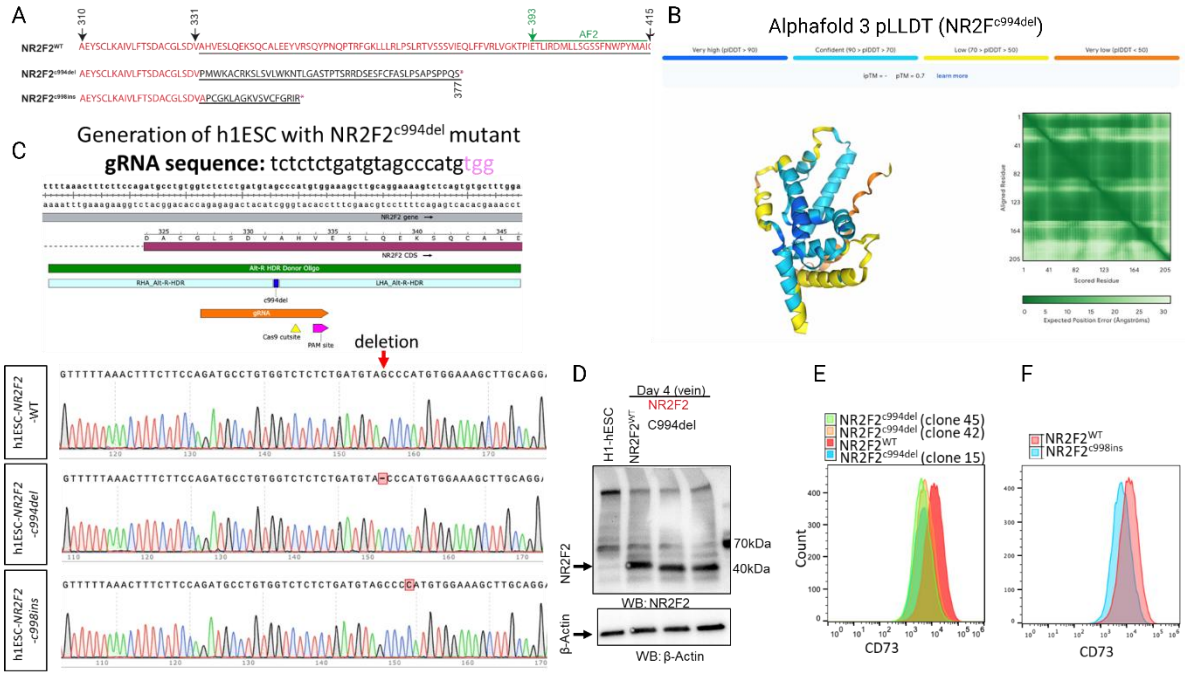

Supp Fig 1: Generation of hESC with NR2F2^{c994del} variant. A Amino acid sequence comparison of NR2F2^{WT} and NR2F2^{c994del}, NR2F2^{c998ins}, an unrelated CRISPR modified cells used as control. **B** The predicted local distance difference tests (pLDDT) for LBD of NR2F2^{c994del}. **C** Generation of H1-hESC mutant clones harboring the NR2F2^{c994del} variant and an unrelated clone NR2F2^{c998ins}. **D** Western blot showing NR2F2^{c994del} protein expression levels compared to wild type in hESC derived venous cells. **E** Histogram plots of CD73 expression in day 4 venous endothelial cells derived from different CRISPR-clones of NR2F2^{c994del} h1ESCs. **F** Histogram plots of CD73 expression in day 4 venous endothelial cells derived from unrelated CRISPR- clones of NR2F2^{c998ins} h1ESCs.

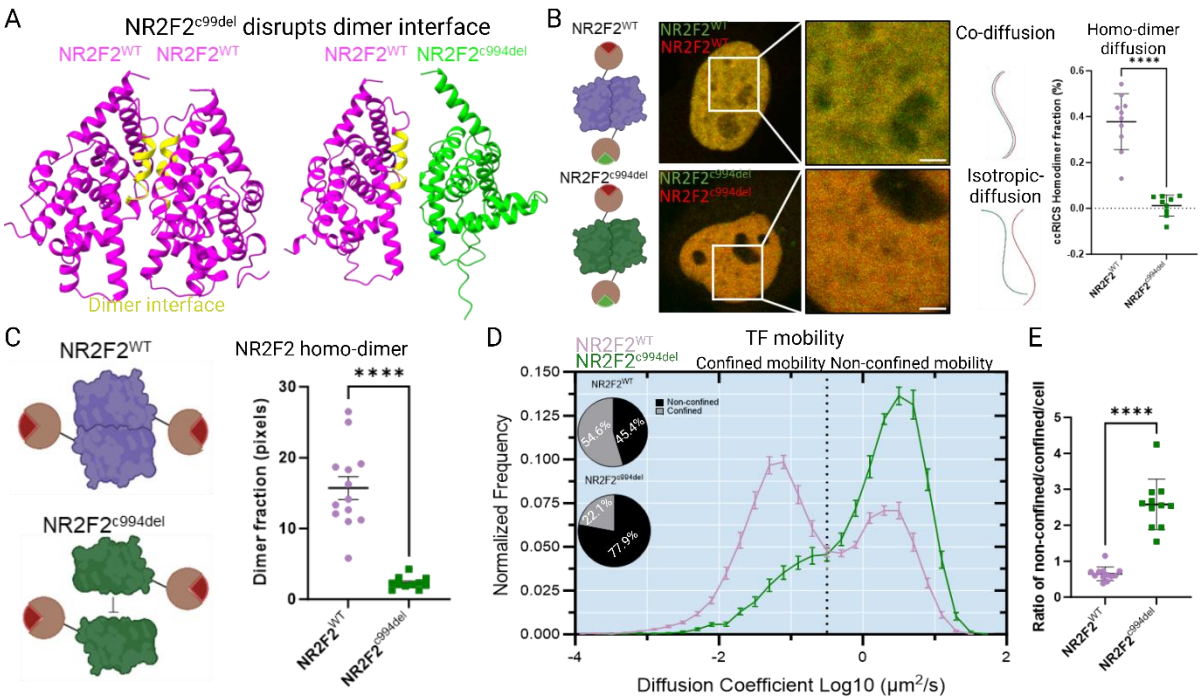

Fig 3: Defects of NR2F2^{c994del} variant cause changes of its molecular behavior. A Modeled dimerization of the LBD of NR2F2^{WT} (purple) and NR2F2^{c994del} (green), dimerization domains (yellow). **B** Cartoon representation of NR2F2^{WT} and NR2F2^{c994del} decorated with Halo-tag (brown) and labelled with either JF549 (green) or JF646 (red). Monomer co-diffusion measured by cross raster imaging correlation spectroscopy (cRICS) to assess homo-dimerisation. **C** Cartoon representations of either NR2F2^{WT} or NR2F2^{c994del} decorated with halotag and its ligand (brown/red), Homo-dimer formation measured by Number and Brightness analysis (N&B). **D** Diffusion mobility graph from single molecule tracking assay comparing NR2F2^{WT} and NR2F2^{c994del}. Pie charts represent the proportion of the population that falls into either confined mobility or non-confined mobility based on diffusion coefficient. **E** Ratio of non-confined to confined molecules per cell from D. For panels B, C, and E, n > 11 cells, statistical significance was determined by Welch's T-test, **** $p < 0.0001$.

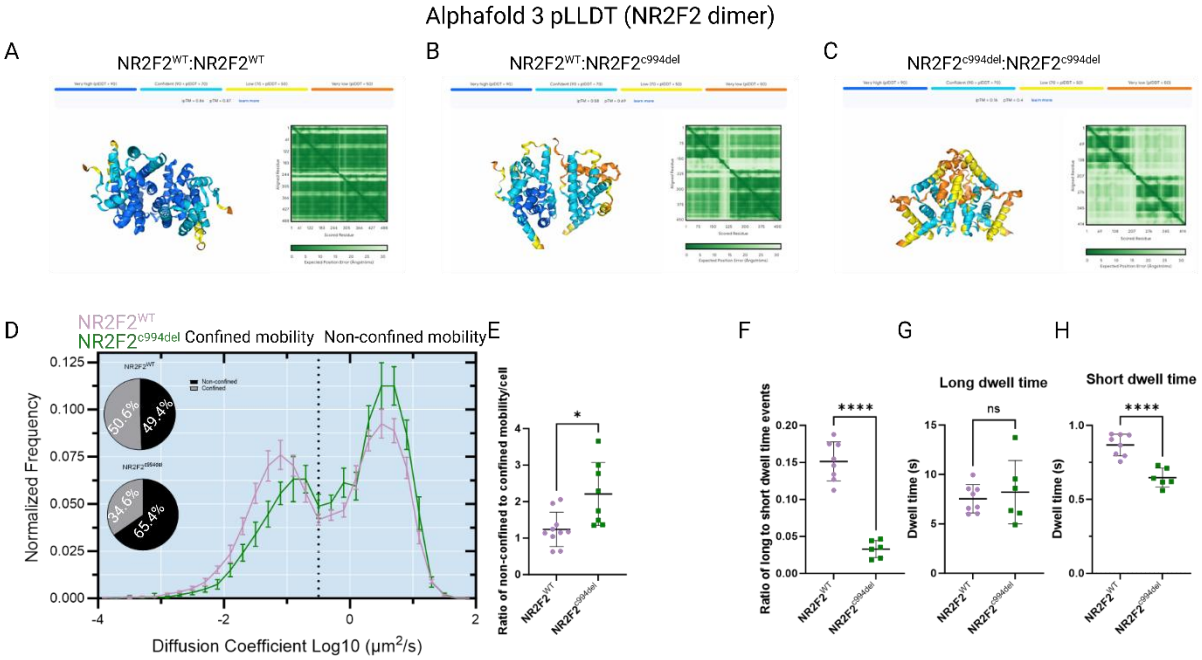

Supp Fig 2: NR2F2 variant behaves similarly in HUVECs. A-C The predicted local distance difference tests (pLDDT) for dimerization of LBD NR2F2^{WT} (A) and dimerization of NR2F2^{WT}, NR2F2^{c994del} (B) and dimerization of NR2F2^{c994del} (note low confidence in the structure). **D** Diffusion mobility graph from single molecule tracking assay comparing NR2F2^{WT} and NR2F2^{c994del} in HUVECs. Pie charts represent the proportion of the population that falls into either confined mobility or non-confined mobility based on diffusion coefficient. **E** Ratio of non-confined to confined molecules per cell from C. **F-H**) Temporal occupancy characteristics. E) Ratio of long to short dwell times, F) long dwell time, and G) short dwell times. For panels D-G, n > 6 cells, statistical significance was determined by Welch's T-test, **** $p < 0.0001$.

Interference mechanism caused by the variant			
N&B (=PPI, oligomeric status) and cRICS (co-diffusion)	**Biophysical Obervation**	**Biological interpretation**	**Fig**
NR2F2 variant homodimer fraction relative to WT	c994del: significantly decreased	c994del does not form homodimers	Fig 3C
SMT (=TF mobility and dwell time)	**Obervation**	**Biological interuption**	**Fig**
NR2F2 variant non-confined mobility (=target gene search pattern) relative to WT	c994del: significantly increased	Majority of c994del molecules diffuse rather than intereact = failure to efficiently select target genome location	Fig 3D,E
NR2F2 variant confined mobility (protein-protein or protien-chromatin interaction) relative to WT	c994del: significantly decreased		

Table 1: Summary of biophysical experiments and biological interpretations for the interference mechanism caused by the variant.

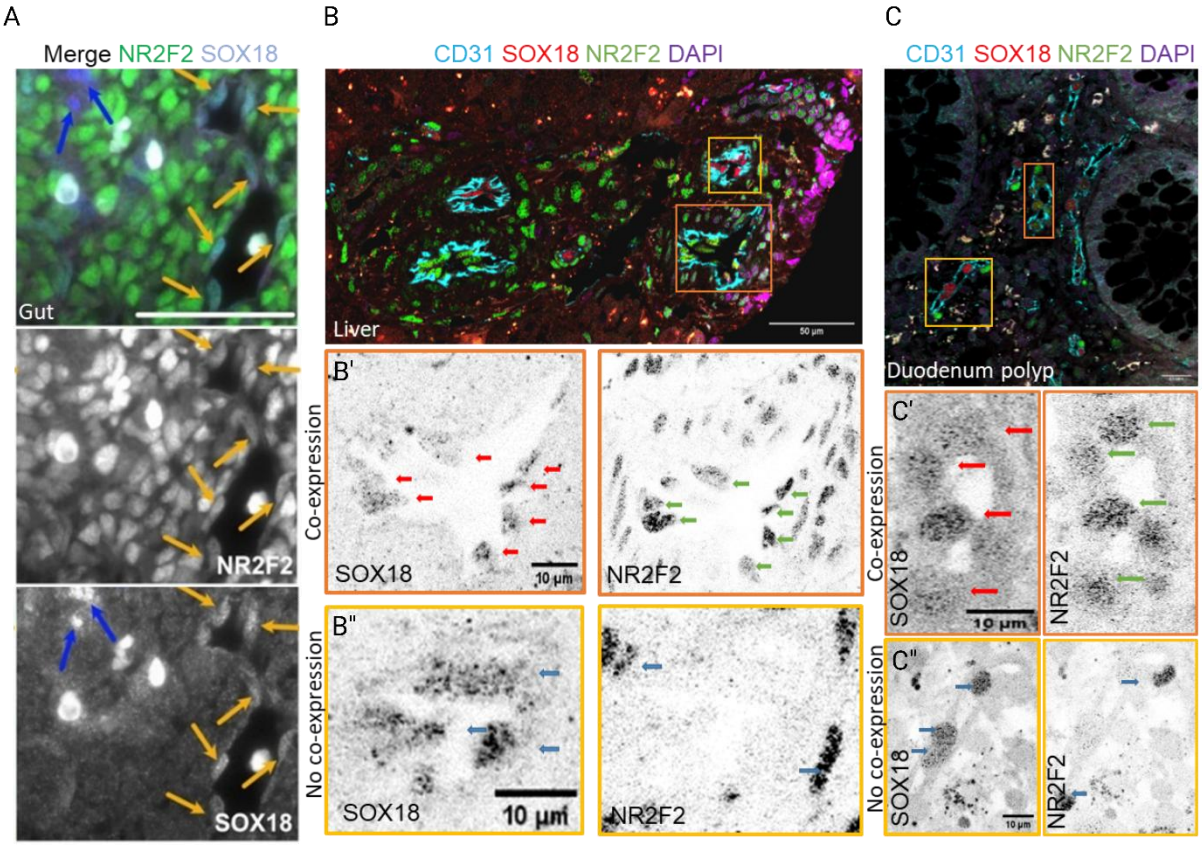

Fig 4: NR2F2 and SOX18 are co-expressed in human ECs during embryogenesis and in the proband tissues. A Immunostaining of sagittal sections from a CS17 human embryo. Co-expression of NR2F2 (green) and SOX18 (blue) in the gut. scale bars 50 µm. **B-B**",and **C-C**" Sections of proband liver (B) and duodenum (C) stained for CD31 (cyan), SOX18 (red arrows), NR2F2 (green arrows), and DAPI (purple). Orange and gold boxes denote zoomed in regions of individual vessels. Orange box represents vessel that shows cells co-expressing both NR2F2 and SOX18 in the same nucleus, whereas the gold box is a vessel with cells either expressing NR2F2 or SOX18. Scale bar = 50µm (B-C) and 10 µm (B'''-C'''').

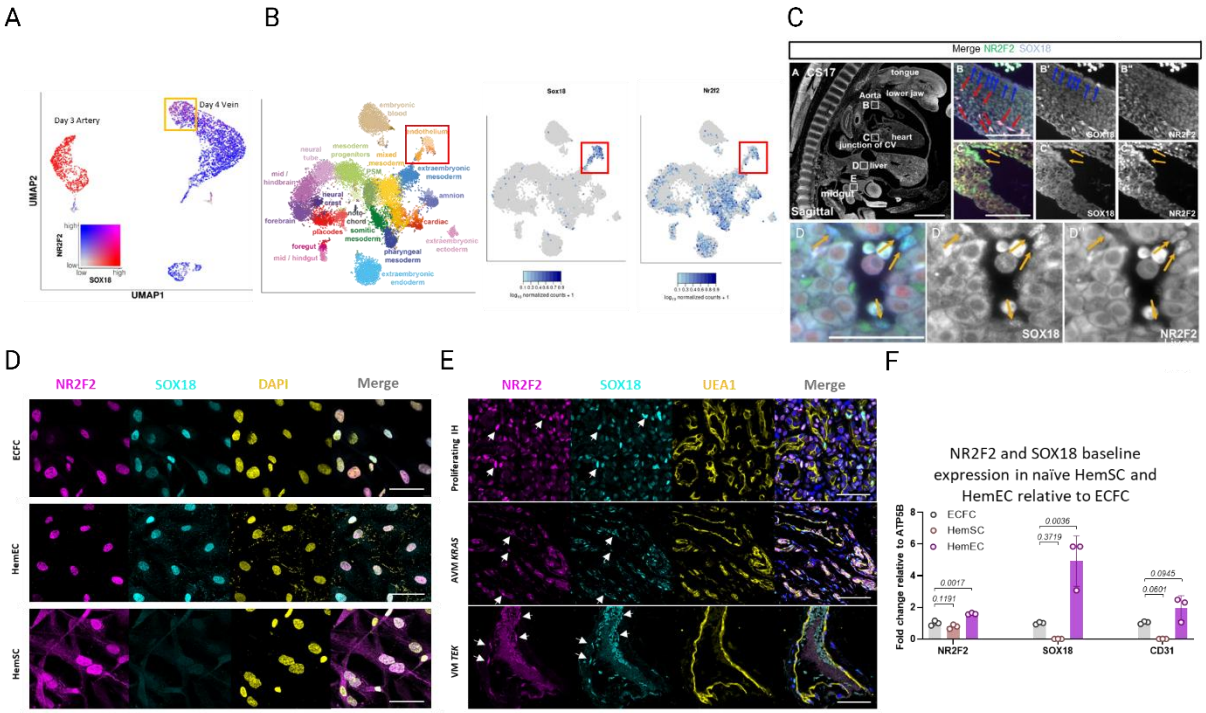

Supp Fig 3: NR2F2 and SOX18 are co-expressed during human venous differentiation and in human neoplasm and vessel malformations. A UMAP of NR2F2 and SOX18 from scRNA-seq dataset from Ang et al. of ECs derived from hESCs. Yellow box denotes venous population expressing both NR2F2 and SOX18. **B** UMAP of NR2F2 and SOX18 from scRNA-seq dataset from Ibarra-Soria et al. of mouse embryo at E8.5. **C** Immunostaining of NR2F2 (green) and SOX18 (blue) in sagittal sections from a CS17 embryo (A-D'''). **D** Immunofluorescent staining of NR2F2 (magenta) and SOX18 (cyan), and nuclei stained with DAPI (yellow) in IH patient-derived hemangioma stem cells (HemSC), hemangioma endothelial cells (HemEC), and ECFC demonstrates nuclear co-expression (scale bars 25 µm). **E** Immunofluorescent staining of NR2F2 (magenta), SOX18 (cyan), and the endothelial marker UEA1 (yellow) in IH, VM, and AVM patient tissue. White arrows denote nuclear co-expression of NR2F2 and SOX18 in EC (scale bars 50 µm). **F** qPCR comparing mRNA levels of NR2F2 and SOX18 in patient-derived HemSC and HemEC relative to ECFC (n=3 biological replicates for HemSC and HemEC, n=3 independent experiments for ECFC; P values were calculated using one-way ANOVA with Dunnett's multiple comparisons test. Data show the mean ± SD.

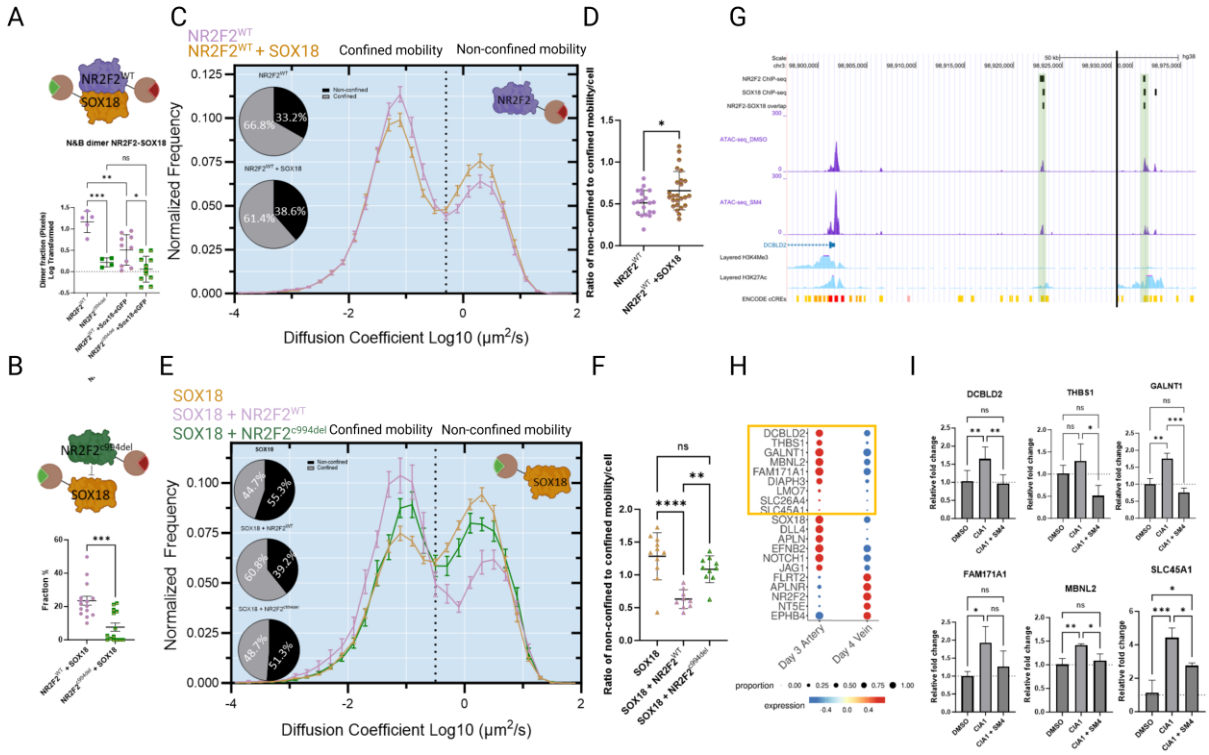

Fig 5: NR2F2 and SOX18 directly interact and co-regulate a specific subset of genes. A Hetero-dimer formation measured by N&B. **B** Hetero-dimer co-diffusion measured by cRICS. **C** Diffusion mobility graph from SMT comparing NR2F2^{WT} (purple) and NR2F2^{WT} + SOX18 (orange). Pie charts represent the proportion of the population that falls into either confined mobility or non-confined mobility based on diffusion coefficient. SMT performed on NR2F2. **D** Ratio of non-confined to confined molecules per cell from C. **E** Diffusion mobility graph from SMT comparing SOX18 (orange), SOX18 + NR2F2^{WT} (purple), and SOX18 + NR2F2^{c994del} (green). Pie charts represent the proportion of the population that falls into either confined mobility or non-confined mobility based on diffusion coefficient. SMT performed on SOX18. **F** Ratio of non-confined to confined molecules per cell from E. **G** Layering of SOX18, NR2F2 ChIP-seq datasets from Sissaoui et al. (NR2F2) and Overman et al. (SOX18) (black bars), with ATAC-seq (purple), histone marks (light blue), and ENCODE cis regulatory elements map (red/orange/yellow) upstream of the DCBLD2 gene locus in HUVECs. Green boxes denote co-binding locations at distal enhancer regions by both NR2F2 and SOX18. **H** Proportion and expression of known arterio-venous identity markers. Yellow box denotes a subset of genes that are regulated by both NR2F2 and SOX18. I) Relative gene expression of treated HUVECS measured by qPCR. For panel D, n > 20 cells, statistical significance was determined by Welch's T-test, * $p < 0.05$. For panels F (n > 9 cells) and I (n = 3 repeats), statistical significance was determined by ANOVA, * $p < 0.05$, ** $p < 0.005$, *** $p < 000.5$, **** $p < 0.0001$.

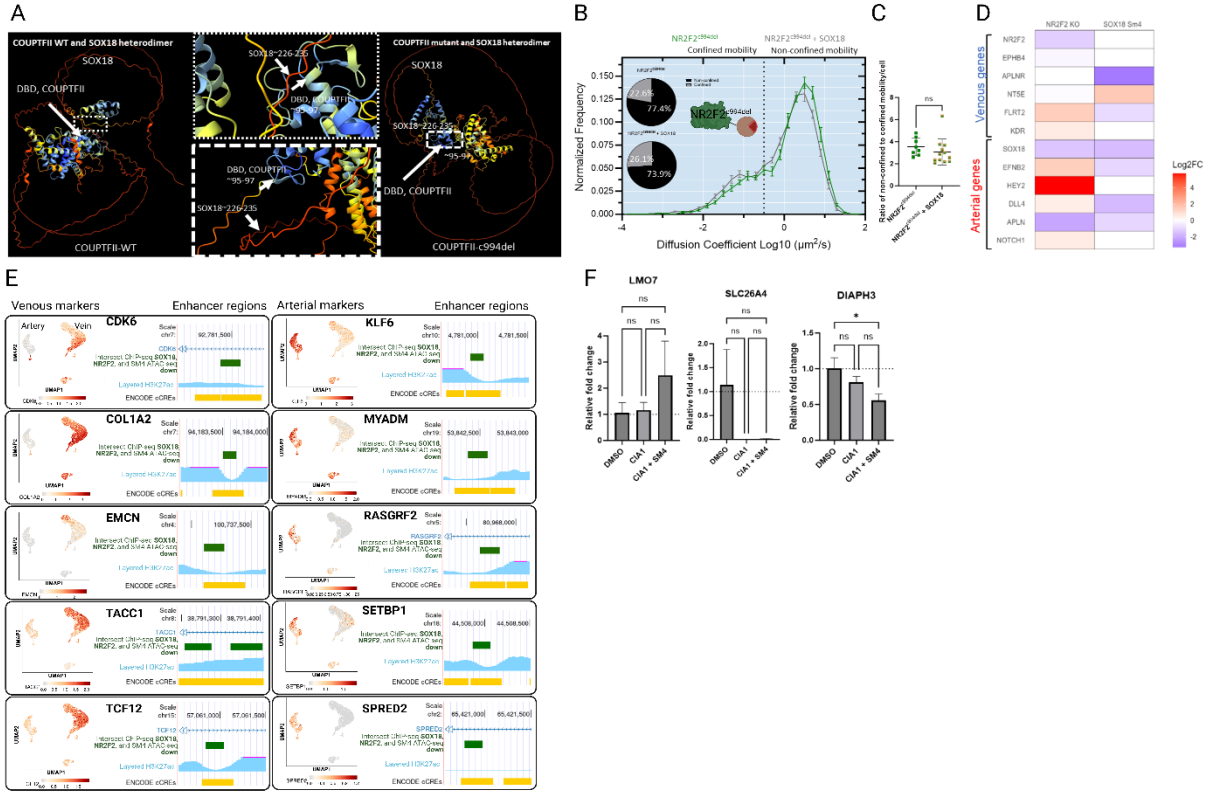

Supp Fig 4: *In silico* modeling of NR2F2 and SOX18 hetero-dimer and molecular imaging show a loss of SOX18 interaction with NR2F2 mutant protein. A Alphafold modeling of NR2F2^{WT} and SOX18 (left) and NR2F2^{c994del} and SOX18 (right). Dimer formation occurs at amino acids 95-97 (DNA binding domain) on NR2F2^{WT} and at amino acid 226-235 (TAD) on SOX18. Modeling shows NR2F2^{c994del} does not directly interact with SOX18 due to changes in folding confirmation. **B** Diffusion mobility graph from SMT comparing NR2F2^{c994del} (green) and NR2F2^{c994del} + SOX18 (grey). Pie charts represent the proportion of the population that falls into either confined mobility or non-confined mobility based on diffusion coefficient. SMT performed on NR2F2. **C** Ratio of non-confined to confined molecules per cell from B. **D** Subset of genes from Supp Table 1 demonstrating either arterial or venous profiles from a publically available scRNA-seq dataset and the genes ATAC-seq differential tracks with and without SM4 treatment in HUVECs. **E-G** SOX18 and NR2F2 co-regulate arterio-venous genes in an antagonistic manner. **E** Expression level of genes from two publically available RNA-seq datasets from Sissaoui et al. (NR2F2) and Overman et al. (SOX18). **F** Relative gene expression of treated HUVECS measured by qPCR. For panels C (n > 8 cells) and F (n = 3 repeats), statistical significance was determined by either Welch's T-test (C) or ANOVA (F), * $p < 0.05$.

Gene	Peak summit coordinates (relative to TSS)
ABHD10	unnamed (-21638)
ACTR2	unnamed (+193040)
ADAMTS16	unnamed (-159060)
ADAMTS20	unnamed (+313335)
ADD3	unnamed (+74218)
ADGRG6	unnamed (+73680)
ADGRV1	unnamed (+329846)
ADK	unnamed (+352070)
AFF4	unnamed (+15894)
AKAP12	unnamed (-235230), unnamed (-172029)
AKR1E2	unnamed (-45262)
ANTXR1	unnamed (+240776)
APH1B	unnamed (-43661)
ARNTL2	unnamed (-40970)
ARRDC3	unnamed (+494716)
ATP23	unnamed (+312217)
ATXN1	unnamed (+415849)
BCAP29	unnamed (+14611)
BEND6	unnamed (-86431)
BET1	unnamed (-179205)
BMP2	unnamed (-205506)
BMPR1A	unnamed (-8600)
BMPR1B	unnamed (-506229)
BTG1	unnamed (+157575)
C1D	unnamed (+145579)
C2CD4A	unnamed (+57487)
C2CD4B	unnamed (+40819)
C2CD6	unnamed (-2315)
C3orf58	unnamed (+799765)
C9	unnamed (+3925)
CALCRL	unnamed (+128858)
CCDC89	unnamed (-39803)
CCKAR	unnamed (-78354)
CD180	unnamed (+133472)
CDK1	unnamed (+49796)
CDK17	unnamed (-45640)
CDK19	unnamed (+277995)
CDK6	unnamed (+52426)
CFAP54	unnamed (-43387)
CGNL1	unnamed (-315564)
CKMT2	unnamed (-265587)
CLVS2	unnamed (+551819)
COL1A2	unnamed (-210981)
COL8A1	unnamed (-667213)
CORO6	unnamed (-104242)
CTXN3	unnamed (+389791)
CYP20A1	unnamed (-132818)
DACH1	unnamed (+961923)
DCBLD2	unnamed (-69573)
DCN	unnamed (-805199)
DDI1	unnamed (-511251)
DEGS1	unnamed (+77013)
DGKD	unnamed (+132701)
DIAPH3	unnamed (+630101)
DLD	unnamed (+58089)
DLGAP1	unnamed (+707568)
DNER	unnamed (+259499)
DPH6	unnamed (+252767)
DST	unnamed (-16945)
DYNC2H1	unnamed (+415754)
EEA1	unnamed (-274177), unnamed (+159638)
EMCN	unnamed (-219098)
ENSG0000(	unnamed (-74562)
EPAS1	unnamed (-229348)
ETAA1	unnamed (+520085)
EXOC6	unnamed (-32324)
FAM133B	unnamed (-191097)
FAM171A1	unnamed (+170260)
FAM198B	unnamed (+11418)
FAM84B	unnamed (-656879)
FASLG	unnamed (+238955)
FAT4	unnamed (+204144)
FBXL2	unnamed (+38592)
FER	unnamed (+357980)
FERMT1	unnamed (-438614)
FILIP1L	unnamed (-45319)
FNIP2	unnamed (+234001)
FRRS1	unnamed (+74373)
FUT10	unnamed (+842068)
FYB1	unnamed (-89978)
GALNT1	unnamed (+380766)
GFPT1	unnamed (+133300)
GMPR	unnamed (+107027)
GRIA2	unnamed (+940914)
GSN	unnamed (+22660)
HAS2	unnamed (-255283)
HHEX	unnamed (+126245)
HIVEP2	unnamed (+570756)
HMG20A	unnamed (+36858)
HMGA2	unnamed (+111844)
ICA1	unnamed (+400634)
ICE2	unnamed (-127075)
IFNE	unnamed (-67115)
IL7	unnamed (-528457)
ITPR2	unnamed (+154052)
KAT6B	unnamed (-323326)
KCNAB1	unnamed (+197013)
KCNMB2	unnamed (-295301)
KCTD12	unnamed (+373578)
KCTD18	unnamed (+103969)
KIAA0319L	unnamed (+51422)
KLF6	unnamed (-995717)
KLHL1	unnamed (-796810)
LAMA4	unnamed (+37243)
LAMB1	unnamed (+54196)
LDB2	unnamed (-119447)
LDB3	unnamed (+79601)
LEAP2	unnamed (+75418)
LINGO1	unnamed (+174958)
LLPH	unnamed (+194464)
LMO7	unnamed (+876154)
LRIG3	unnamed (+666728)
LRRC40	unnamed (+160570)
LRRC7	unnamed (+284875)
LSAMP	unnamed (-806917)
MAGEB5	unnamed (+572469)
MAML2	unnamed (+33917)
MAP2K1	unnamed (+19076)
Mar-07	unnamed (-1537)
MAST4	unnamed (+466966)
MBNL1	unnamed (-241910)
MKKS	unnamed (+80596)
MRPL17	unnamed (-12191)
MTAP	unnamed (-253115)
MTFR2	unnamed (+214477)
MTHFD1L	unnamed (+139090), unnamed (+202291)
MTMR2	unnamed (-384968)
MXI1	unnamed (-125425)
MYADM	unnamed (-26928)
MYC	unnamed (+7016)
NANOGP8	unnamed (-208291)
NDUFA4	unnamed (+782912)
NFIA	unnamed (+206059)
NFIB	unnamed (-59342)
NFKBIZ	unnamed (+329473)
NLRP12	unnamed (-18084)
NMT2	unnamed (-32106)
NRG1	unnamed (+82719)
NUDT4	unnamed (-174375)
NUDT7	unnamed (-128340)
NVL	unnamed (+70203)
OR1K1	unnamed (+19737)
OR2AG2	unnamed (+76384)
PALM2	unnamed (+247400)
PALMD	unnamed (+45477)
PDCD1LG2	unnamed (-684)
PDCL	unnamed (+8771)
PDE4D	unnamed (+330937)
PDE7B	unnamed (+184138)
PDLIM5	unnamed (+93593)
PEG10	unnamed (+41281)
PHLDB2	unnamed (+98217)
PID1	unnamed (-222974)
PJA2	unnamed (+304192)
PLEKHA2	unnamed (-110049), unnamed (-109925
PLEKHG7	unnamed (+33204)
PLSCR1	unnamed (+37920)
PLSCR2	unnamed (-37643), unnamed (+191162)
PLSCR4	unnamed (-26960)
POU5F1B	unnamed (-199018)
PPP1R9A	unnamed (-209986)
PPP3CA	unnamed (+610289)
PRICKLE1	unnamed (-648816)
PRKCE	unnamed (+416280)
PXN	unnamed (-25913)
QDPR	unnamed (+493978)
RAB3C	unnamed (+979821)
RAB8B	unnamed (+44424)
RAP1GAP	unnamed (-144916)
RAPGEF2	unnamed (-264598)
RASA2	unnamed (-829)
RASGRF2	unnamed (+7065)
RASGRP1	unnamed (-431706)
RCOR1	unnamed (+62663)
RERE	unnamed (+104741)
RHOBTB1	unnamed (+115997)
RORA	unnamed (+21243)
RPA3	unnamed (-143040)
RPIA	unnamed (+45928)
RPRD1A	unnamed (+32250)
SEMA6D	unnamed (-252013)
Sep-11	unnamed (-500278)
SETBP1	unnamed (-172934)
SGO1	unnamed (-70064)
SHROOM3	unnamed (+14459)
SIRT4	unnamed (-10637)
SLC12A2	unnamed (-44931)
SLC22A16	unnamed (-60680)
SLC26A4	unnamed (-65265)
SLC38A2	unnamed (-57589)
SLC38A4	unnamed (+395541)
SLC45A1	unnamed (+394898)
SMCO2	unnamed (-4319)
SNAP25	unnamed (+134796)
SNAPC5	unnamed (+91920)
SNCA	unnamed (+288303)
SNRPE	unnamed (+27452)
SNTB2	unnamed (+37991)
SNX9	unnamed (-287268)
SOX13	unnamed (-184537)
SPATS2L	unnamed (+97144)
SPRED2	unnamed (+11300)
SS18	unnamed (+572392)
SSH2	unnamed (+202952)
SSPN	unnamed (+483650)
SSR3	unnamed (+237588)
STAT1	unnamed (-17197)
STAT4	unnamed (+119813)
STK38L	unnamed (+47910)
STMN2	unnamed (-277172)
STOM	unnamed (+47752)
SUCNR1	unnamed (+152487)
SYTL2	unnamed (+85049)
TACC1	unnamed (+4038), unnamed (+4162)
TBC1D19	unnamed (-15100)
TBC1D23	unnamed (-101180)
TCF12	unnamed (+142318)
TGIF1	unnamed (+296090)
THBS1	unnamed (-584581)
TIGD2	unnamed (+438512)
TLE3	unnamed (-592919)
TM2D1	unnamed (+437220)
TMEM2	unnamed (+623377)
TNFSF18	unnamed (+152990)
TRAF3	unnamed (-122152)
TRDN	unnamed (+89303)
TRPM3	unnamed (-23909)
TTC26	unnamed (+20234)
TUBE1	unnamed (-129959)
TXN	unnamed (+228801)
UACA	unnamed (+72498)
UBE2R2	unnamed (-2551)
UBN2	unnamed (-77473)
UBP1	unnamed (+124364)
USP40	unnamed (+78382)
USP48	unnamed (+18649)
UTRN	unnamed (+58180)
WDR12	unnamed (-193896)
ZDHHC14	unnamed (+154863)
ZDHHC21	unnamed (+320462)
ZHX2	unnamed (-884721)
ZMYM4	unnamed (+237024)
ZNF521	unnamed (-166081)
ZPLD1	unnamed (-256028)
ZSWIM2	unnamed (-470432)

Supp Table 1: Peak to gene analysis of assigned enhancers relative to TSS from intersected peaks with ATAC-seq and ChIP-seq datasets.

Gene	Cell type
ARHGEF37	venous
ATG16L2	venous
BBS12	venous
CHST2	venous
CMSS1	pre venous/ venous/ arterial
DCBLD2	pre arterial pre venous
DDR2	pre venous
DEK	pre venous/ arterial
DIAPH3	pre venous
DUSP4	pre venous/ arterial
EDN1	arterial / venous
ERRFI1	pre venous/ arterial
FAM171A1	arterial / venous
FBXO5	pre arterial pre venous
FHL2	pre arterial
FKBP5	venous
GALNT1	pan endothelial
GATA6	pre venous
GIMAP4	venous
HIST1H2AE	venous
HIST1H2BB	low
HIST1H2BG	low
HIST1H2BJ	venous
HIST1H3C	low venous
HIST1H4E	venous
HIST1H4H	venous/artery
HTR1B	pre venous
IL20RB	low
KCNAB2	low
KIF20B	pre arterial pre venous
LMO7	pre venous low
MBNL1	venous
MEF2C	venous
MMP10	low
MN1	pre venous / venous

Gene	Cell type
MXI1	venous
NRP1	arterial/ venous
NTN4	pre venous
OGT	venous
OTOGL	low
PDE3A	pre venous
PDLIM3	pre venous
PIK3R3	pre venous / venous
PKN2	pre venous / venous
PPIB	pan endothelial high
RALGPS2	pre arterial / pre venous / venous
RFC3	pre venous / venous
RGCC	arterial / venous
SCFD2	venous
SERBP1	venous
SESN1	venous
SHCBP1	arterial / pre venous
SLC1A4	arterial
SLC7A11	arterial / pre venous
SLC26A4	venous
SLC38A1	arterial / venous
SLC45A1	venous
SPRY1	arterial / hemogenic
STC1	pre arterial
STC2	arterial
SYNE1	pre venous/ venous
TAPT1	venous
THBS1	pre arterial pre venous
TMEM47	pre venous
TMEM170E	venous
TNRC6A	venous/ arterial
TRAF3IP2	arterial / venous
TUBE1	arterial venous
YAE1D1	pre venous

Supp Table 2: Subset of genes from Supp Table 1 that have arterial or venous specific profiles.

Gene	HUVEC (log2 fold)	Gene	HUVEC (log2 fold)
STC2	3.11	RALGPS2	0.03
KLF4	2.29	FAM171A1	0.01
VEGFA	2.15	PDLIM3	0.00
SLC1A4	2.09	TNRC6A	0.00
SLC7A11	1.77	HIST1H3E	-0.02
LMO7	1.57	KCNAB2	-0.03
ERRFI1	1.47	MN1	-0.05
SLC38A1	1.28	TMEM170B	-0.08
TUBE1	1.24	YAE1D1	-0.10
DDR2	1.08	GIMAP4	-0.10
STC1	0.91	HIST1H2AE	-0.18
FHL2	0.87	EDN1	-0.22
DCBLD2	0.86	FKBP5	-0.24
SYNE1	0.71	PDE3A	-0.26
OGT	0.71	THBS1	-0.28
TMEM47	0.68	GATA6	-0.28
BBS12	0.60	GALNT1	-0.30
ATG16L2	0.50	FBXO5	-0.33
MXI1	0.43	SCFD2	-0.40
CMSS1	0.41	PIK3R3	-0.51
DEK	0.38	HTR1B	-0.57
TAPT1	0.37	DIAPH3	-0.57
CHST2	0.34	HIST1H2BG	-0.63
DUSP4	0.32	RFC3	-0.66
ARHGEF37	0.28	HIST1H4H	-0.68
MEF2C	0.27	KIF20B	-0.81
RGCC	0.24	HIST1H2BB	-0.83
MBNL1	0.22	HIST1H2BJ	-0.83
NTN4	0.21	SHCBP1	-1.14
SPRY1	0.20	HIST1H3C	
PKN2	0.19	IL20RB	
NRP1	0.17	OTOGL	
SESN1	0.16	SLC26A4	
SERBP1	0.16	MMP7	
MMP10	0.13	VCAM1	
NOTCH1	0.08		
TRAF3IP2	0.07		
IL33	0.06		
HIST1H4E	0.06		
SLC45A1	0.06		
PPIB	0.04		

Supp Table 3: Relative expression of genes from Supp Table 2 measured by qPCR.

Interplay between SOX18 and NR2F2			
N&B (=PPI, oligomeric status) and cRICS (co-diffusion)	**Biophysical Obervation**	**Biological interpretation**	**Fig**
SOX18 /NR2F2 heterodimer fraction relative to NR2F2 WT only	WT + SOX18: significantly decreased	SOX18 inteferes with NR2F2 WT homodimer formation	Fig 5A
SOX18 /NR2F2 heterodimer fraction relative to c994del only	c994del + SOX18: no change	c994del does not form heterodimers with SOX18	Fig 5A
SMT	**Obervation**	**Biological interuption**	**Fig**
NR2F2 non-confined mobility in presence or absence of SOX18	NR2F2 WT + SOX18: decreased proportion	NR2F2 WT /SOX18 interplay leads to a more diffusive behaviour of NR2F2, possibly via sequestration away from chromatin or competitive binding	Fig 5C,D
NR2F2 confined mobility (protein-protein or protien-chromatin interaction) in presence or absence of SOX18	NR2F2 WT + SOX18: increased proportion		
SOX18 non-confined mobility (diffusing) in presence or absence of NR2F2 WT	SOX18+NR2F2 WT: decreased proportion	NR2F2WT stabilizes SOX18 binding leading to increased confined fraction nad less diffusive behaviour possibly via increase in SOX18 homodimer formation	Fig 5E,F
SOX18 confined mobility (protein-protein or protein-chromatin interaction) in presence of NR2F2 WT	SOX18+ NR2F2 WT: increased proportion		
SOX18 non-confined mobility (diffusing) in presence or absence of NR2F2 variant	c994del + SOX18: no change= no interaction with SOX18		Fig 5E,F
SOX18 confined mobility (protein-protein or protein-chromatin interaction) in presence of NR2F2 variant	c994del + SOX18: no changeno change= no interaction with SOX18		
non-confined mobility (diffusing) relative to c994del	c994del + SOX18: no changeno change= no interaction with SOX18	In a NR2F2WT/Variant heterozygous situation, c994del variant population lessen the interplay NR2F2 WT/ SOX18 and therefore favors more SOX18-bound to chromatin	Supp Fig 4B,C
confined mobility (protein-protein or protien-chromatin interaction) relative to c994del	c994del + SOX18: no changeno change= no interaction with SOX18		

Table 2: Summary of biophysical experiments and biological interpretations of NR2F2 and SOX18 interactions.

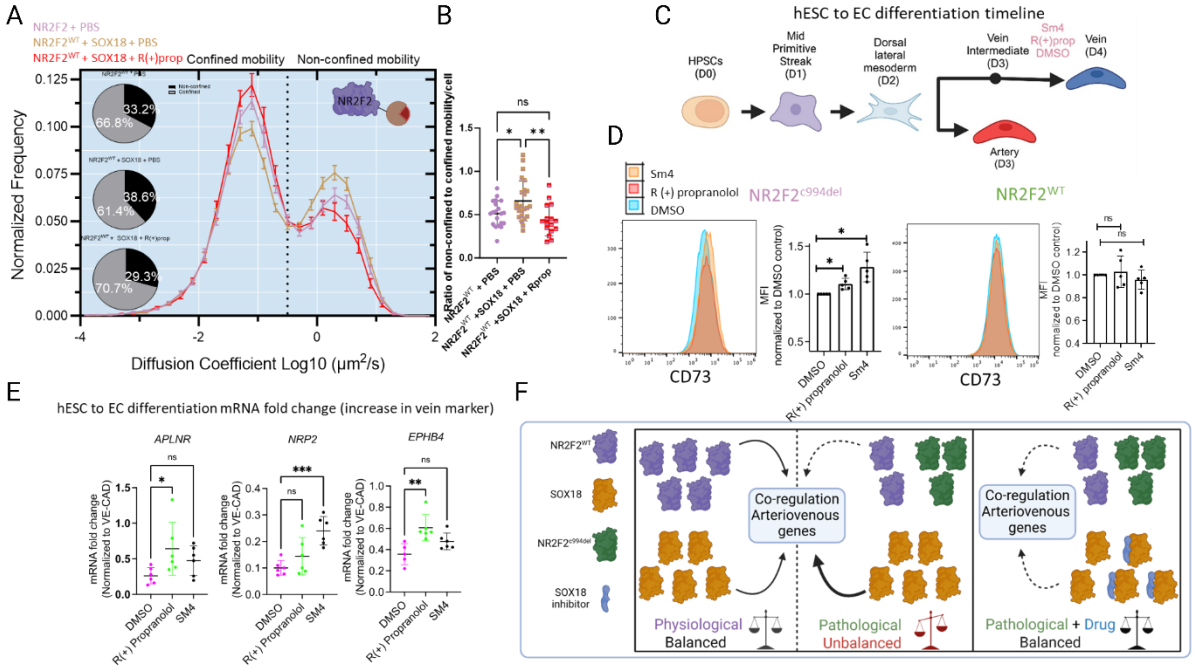

Fig 6: Molecular mechanism of propranolol rescue of venous defects is SOX18-dependent. A SMT performed on NR2F2. Diffusion mobility graph from SMT comparing $NR2F2^{WT}$ + PBS (purple), $NR2F2^{WT}$ + SOX18 + PBS (orange), and $NR2F2^{WT}$ + SOX18 + R(+)prop (red). Pie charts represent the proportion of the population that falls into either confined mobility or non-confined mobility based on diffusion coefficient. **B** Ratio of non-confined to confined molecules per cell from A. **C** Schematic of hESC to EC differentiation timeline with drug treatment. **D** Histogram plots of venous derived populations, WT c994del and corresponding quantification of MFI. An increase of the CD73 expression occurs in the presence of SOX18 blockers despite the NR2F2 mutation. **E** Relative gene expression measured by qPCR from day 4 venous cells. **F** Model of the proposed molecular mechanism underlying the $NR2F2^{c994del}$ rescue. Under physiological conditions in venous cells, NR2F2 and SOX18 are co-expressed at a specific ratio. This ratio allows for an antagonistic co-regulation of arteriovenous markers in vein ECs that is essential to maintain venous identity. In the probands's scenario NR2F2 heterozygous mutation alters the proper ratio between $NR2F2^{WT}$ and SOX18 that then becomes unbalanced in favor of SOX18 activity, leading to an upregulation of arterial markers and a perturbation of venous identity. Treatment with a SOX18 inhibitor enables the restoration of balance between SOX18 and NR2F2 activity, allowing a smaller proportion of both TF populations to function properly at physiological levels. Panels B ($n > 16$ cells) and E ($n = 3$ repeats), statistical significance was determined by ANOVA, * $p < 0.05$, ** $p < 0.005$, *** $p < 000.5$.

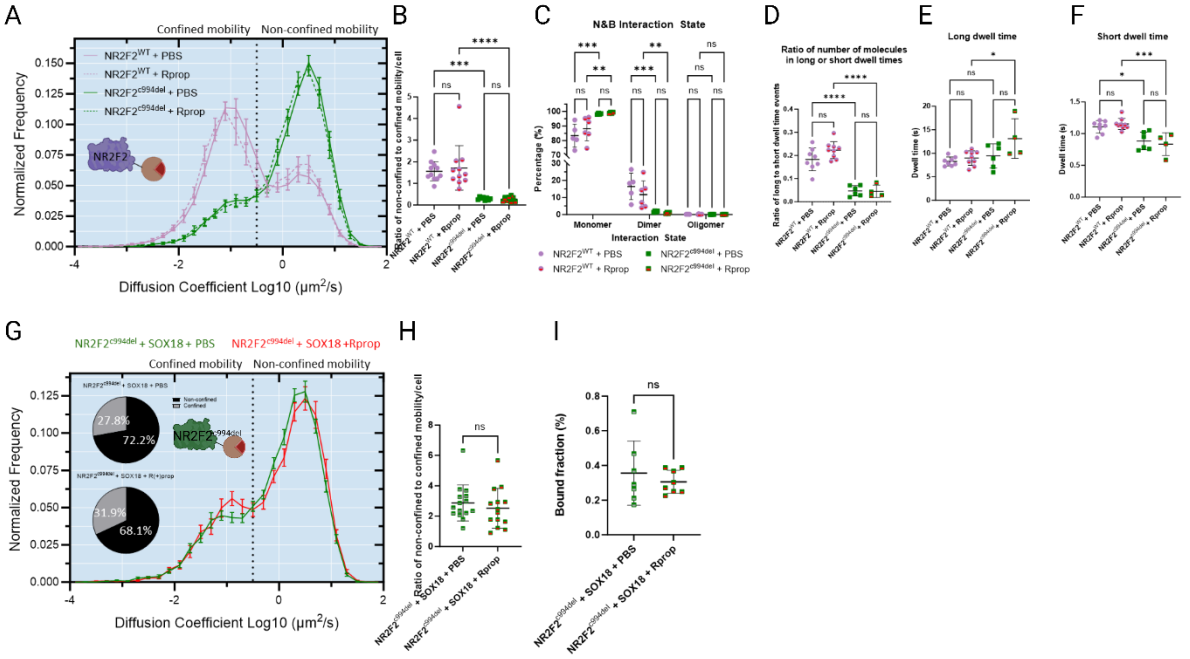

Supp Fig 5: R(+)propranolol does not interfere directly with NR2F2 activity. A Diffusion mobility graph from SMT comparing NR2F2^{WT} + PBS (purple), NR2F2^{WT} + Rprop (purple, hashed), NR2F2^{c994del} + PBS (green), and NR2F2^{c994del} + Rprop (green, hashed). SMT performed on NR2F2. **B** Ratio of non-confined to confined molecules per cell from A. **C** Monomer, dimer, and oligomeric states measured by N&B. **D-F** Temporal occupancy characteristics. **D** Ratio of long to short dwell times, **E** long dwell time, and **F** short dwell times. **G** Diffusion mobility graph from SMT comparing NR2F2^{c994del} + SOX18 + PBS (grey), and NR2F2^{c994del} + SOX18 + Rprop (red). SMT performed on NR2F2. **H** Ratio of non-confined to confined molecules per cell from G. **I** Hetero-dimer formation measured by RICS between NR2F2^{c994del} + PBS and NR2F2^{c994del} + Rprop when SOX18 is present. For panels B (n > 8 cells), C-E (n > 5 cells), F (n > 5 cells), H (n > 14 cells), and I (n > 8 cells), statistical significance was determined by ANOVA (B-E), Two-way ANOVA (F), and Welch's T-test (H-I), * $p < 0.05$, ** $p < 0.005$, *** $p < 000.5$, **** $p < 0.0001$.

Drug mode of action			
N&B (=PPI, oligomeric status) and cRICS (co-diffusion)	**Biophysical Obervation**	**Biological interpretation**	**Fig**
NR2F2 WT homodimer fraction relative to WT + PBS	WT + Rprop: no change	Rprop does not affect NR2F2 WT dimer formation	Supp Fig 5C
NR2F2 WT homodimer fraction relative to c994del+ PBS	c994del + Rprop: no change	Rprop does not affect c994del oligomeric status	Supp Fig 5C
SMT	**Obervation**	**Biological interuption**	**Fig**
non-confined mobility (diffusing) of NR2F2 Wt or NR2F2 variant in presence or absence of R-propranolol	no change caused by drug treatment	Rprop does not affect NR2F2 WT or variant mobility	Supp Fig 5A,B
confined mobility (diffusing) of NR2F2 Wt or NR2F2 variant in presence or absence of R-propranolol	no change caused by drug treatment		
NR2F2 non-confined mobility (diffusing) in presence or absence of SOX18 with or without Rpropranolol	Adding SOX18 leads to increased NR2F2 diffusion, effects that is counteracted by Rpropranolol	Rpropranolol rescues NR2F2 WT changes of behaviour that are caused by SOX18	Fig 6A,B
NR2F2 confined mobility (diffusing) in presence or absence of SOX18 with or without Rpropranolol	Adding SOX18 leads to decreased NR2F2 bound fraction, effects that is counteracted by Rpropranolol		
NR2F2 variant non-confined mobility (diffusing) in presence of SOX18 with or without Rpropranolol treatment	c994del + SOX18 +/- Rprop: no change	Inhibition of SOX18 does not impact variant mobility	Supp Fig 5G,H
NR2F2 variant confined mobility (protein-protein or protien-chromatin interaction) in presence of SOX18 with or without Rpropranolol treatment	c994del + SOX18 +/- Rprop: no change		

Table 3: Summary of biophysical experiments and biological interpretations investigating drugs effect on NR2F2 and SOX18.